

**Multimodal Investigation of fMRI and fNIRS derived Breath
Hold BOLD Signals with an Expanded Balloon Model**

by

Uzay Emrah Emir

B.S., in Electrical and Electronics Engineering, Ege University, 2001

M.S., in Biomedical Engineering, Boğaziçi University, 2003

Submitted to the Institute of Biomedical Engineering

in partial fulfillment of the requirements

for the degree of

Doctor

of

Philosophy

Boğaziçi University

January 2008

ACKNOWLEDGMENTS

First of all, I would particularly like to thank my supervisors Assistant Prof. Dr. Akın and Assoc. Prof. Dr. Öztürk. They have been extremely helpful with continuous guidance and support throughout this research, and patiently proof-reading all my manuscripts.

I am very grateful to Prof. Dr. Demiralp. He has been a constant source of motivation, guidance, and insight. I would like to express my gratitudes to Prof. Dr. Ademođlu for his collaborations and invaluable guidance. I also thank Assoc. Prof. Dr. Aydın and Dr. Diđer for their supports to access MRI instrument at Istanbul Faculty of Medicine and Acibadem Hospital, respectively.

I would also like to thank Ömer Şaylı, Zübeyir Bayraktarođlu, Özlem ÖZMEN OKUR and Murat Tümer. It has been a great pleasure to work and have fun with you.

Last, but not least, I would like to thank my wife, Serap Emir, for her constant support and encouragement throughout my studies.

ABSTRACT

Multimodal Investigation of fMRI and fNIRS derived Breath Hold BOLD Signals with an Expanded Balloon Model

Multimodal investigation of blood oxygenation level-dependent (BOLD) signal, using both functional near infrared spectroscopy (fNIRS) and functional magnetic resonance imaging (fMRI), may give further insight to the underlying physiological principles and the detailed transient dynamics of the vascular response. Utilizing a breath hold task (BHT), we measured deoxy-hemoglobin (HbR) and oxy-hemoglobin (HbO) changes via fNIRS and blood oxygen level dependent (BOLD) changes by fMRI. Measurements were taken in four volunteers asynchronously and carefully aligned for comparative analysis. In order to describe the main stimulus in BHT, partial pressure of carbon dioxide (PaCO_2) parameter was integrated into the balloon model as the driving function of cerebral blood flow (CBF) which led to the development of an expanded balloon model (EBM). During BHT, the increase in HbR was observed later than the BOLD peak and coincided temporally with its post stimulus undershoot. Further investigation of these transients with PaCO_2 integrated balloon model suggests that post stimulus undershoot measured by fMRI is dominated by slow return of cerebral blood volume (CBV). This was confirmed by fNIRS measurements. In addition, BOLD signal decreased with the increase of the initial level of PaCO_2 derived from EBM, indicating an effect of basal CBF level on the BOLD signal. In conclusion, a multimodal approach with an appropriate biophysical model gave a comprehensive description of the hemodynamic response during BHT.

Keywords: Functional near-infrared spectroscopy, Functional magnetic resonance imaging, BOLD signal, Partial pressure of CO_2 , Balloon model, Post stimulus undershoot.

ÖZET

İYKÖS ve İMRG ile elde edilmiş Nefes Tutma KOSB İşaretlerinin Genişletilmiş Balon Modeliyle İncelenmesi

Kanın Oksijenlenme Seviyesi Bağımlılığı (KOSB) işaretinin İşlevsel Yakın Kıızıl Ötesi Spektroskopi (İYKÖS) ve İşlevsel Manyetik Rezonans Görüntüleme (İMRG) gibi birden çok aletle incelenmesi, sinir-damar tepkisinin dalgalanma dinamikleri ve altında yatan fizyolojik temeller hakkında daha fazla bilgi verebilir. Bu çalışmada nefes tutma görevi (NTG) kullanarak, oksijensiz hemoglobin (HbR) ve oksijenli hemoglobin (HbO) değişimleri İYKÖS ile ölçülürken, KOSB işareti İMRG ile ölçüldü. Ölçümler ayrı zamanlarda dört gönüllüden alındı. Her iki aletten gelen veriler dikkatlice zamansal olarak eşleştirildi. NTG'de temel uyarımı tanımlayabilmek için karbondioksit kısmi basınç (PaCO_2) değişkeni balon modelde beyin kan akışı (BKA) değişkenini hesaplayacak şekilde eklendi. Böylece genişletilmiş balon model (GBM) geliştirildi. NTG sırasında KOSB tepesinden sonra ölçülen HbR artışının KOSB'daki uyarım sonrası düşüşe zamansal olarak denk geldiği gözlemlendi. Bu dalgalanmaların PaCO_2 eklenmiş balon model ile detaylı analizi, KOSB'da görülen uyarım sonrası düşüşün beyin kan hacminden (BKH) kaynaklandığını önermektedir. Bu bulgu İYKÖS ölçümleriyle de desteklenmektedir. Bunlara ek olarak, GBM'den elde edilen PaCO_2 başlangıç seviyesi artışı, KOSB işaretinde azalışa neden olmaktadır ki bu da temel BKA seviyesinin KOSB işareti üzerindeki etkisi ile açıklanabilmektedir. Sonuç olarak, birden fazla aletli ölçüm yaklaşımı ile bunlara uygun biyofiziksel model, NTG sırasında beyin kanlanma tepkisi hakkında kapsamlı bilgi vermektedir.

Anahtar Sözcükler: İşlevsel Yakın Kıızıl Ötesi Spektroskopi, İşlevsel Manyetik Rezonans Görüntüleme, KOSB işareti, Karbondioksit kısmi basıncı, Balon modeli, Uyarım sonrası düşüş.

TABLE OF CONTENTS

ACKNOWLEDGMENTS	iii
ABSTRACT	iv
ÖZET	v
LIST OF FIGURES	viii
LIST OF TABLES	xii
LIST OF SYMBOLS	xiii
LIST OF ABBREVIATIONS	xiv
1. Introduction	1
1.1 Motivation and Objectives	1
1.2 Outline of the Thesis	2
2. Physiological Background	4
2.1 Brain Anatomy	4
2.1.1 Major Regions of The Brain and Their Functions	4
2.1.2 Functional Organization of The Brain	6
2.1.3 Cellular Architecture of The Brain	7
2.2 Brain Energy Metabolism	8
2.2.1 Coupling of Brain Energy Metabolism to Blood Flow	11
2.2.1.1 Adenosine and Positively Charged Ions	11
2.2.2 Blood Gases and Cerebral Blood Flow	12
3. Neuroimaging Techniques	16
3.1 Functional Magnetic Resonance Imaging	16
3.1.1 DW-EPI	23
3.1.2 ASL	25
3.2 fNIRS	26
3.2.1 Principles of Near-Infrared Spectroscopy	26
3.2.1.1 Absorption	27
3.2.1.2 Scattering	31
3.2.1.3 Modified Lambert Beer Law, Hb, HbO Calculations	31
3.3 Other Neuroimaging Modalities	34

3.3.1	EEG/MEG	34
3.3.2	PET	35
3.4	Multimodality Neuroimaging Approaches	35
4.	Physiological Background of BOLD Signal and Balloon Model	38
4.1	BOLD Physiology	38
4.1.1	Initial Dip	39
4.1.2	Positive BOLD	41
4.1.3	Post Stimulus Undershoot	41
4.2	Balloon Model	42
4.2.1	Balloon Model Improvements	48
5.	Multimodal Investigation of fMRI and fNIRS derived Breath Hold BOLD Signals with an Expanded Balloon Model	51
5.1	Introduction	51
5.2	Methods	52
5.2.1	Subjects and Study Design	52
5.2.2	fNIRS	54
5.2.3	fMRI	54
5.2.4	Balloon Model	55
5.3	Results	57
6.	Discussion	63
6.0.1	Effects of Breath Hold on Cerebral Hemodynamics	63
6.0.2	BOLD and fNIRs Vasoreactivity Transients During Breath Hold	64
7.	Conclusion	68
	APPENDIX A. Published Papers During the PhD Studies	70
A.1	Journal Papers	70
A.2	Conference Proceedings	70
	REFERENCES	72

LIST OF FIGURES

Figure 2.1	An illustration of skin, skull, meninges and CSF [4].	5
Figure 2.2	Major parts of the brain - cerebrum, cerebellum, brainstem [4].	5
Figure 2.3	Functional areas of cerebral cortex [4].	7
Figure 2.4	Schematic representation of cytological relations existing among capillaries, astrocytes and neurons [5].	8
Figure 2.5	The Glucose metabolism. Glucose can be derived from glycogen. Through glycolysis, glucose is transformed into pyruvate, which yields 2 ATP. Lactate is anaerobically formed from pyruvate. With oxygen, pyruvate is metabolized in the citric acid cycle, which yields another 34 ATP.	9
Figure 2.6	An illustration of astrocyte-neuron lactate shuttle [5].	10
Figure 2.7	Dynamic components of coupling between functional activity, metabolism and blood flow in the brain. The activity dependent element is represented by K^+ , the metabolic element by H^+ and adenosine [19].	12
Figure 2.8	The response of cerebral circulation to changes in arterial oxygen tension [21].	13
Figure 2.9	Cerebral vasodilator activity of CO_2 [26].	15
Figure 3.1	Cross sectional brain image. From left to right: proton density weighted, T_1 weighted, T_2 weighted images.	17
Figure 3.2	Magnetic field distortion due to paramagnetic HbR and diamagnetic HbO. There is no distortion around HbO. However, There is a dipole field distortion in surrounding of HbR.	18
Figure 3.3	fMRI pulse sequences. (a) SE-EPI sequence. Spin echo formed by the 90-180 pulse pair at the center of the EPI readout period, which ordinarily is the center of k-space. (b) GE-EPI sequence. In this sequence, EPI readout period follows a single radiofrequency pulse, whose flip angle is 90.	20

Figure 3.4	Plot of Signal vs. TE, using Eq. 3.11, S_o equals to 1. The two curves represent typical values of R_2^* in the brain. The difference in relaxation rates represent typical differences between resting (20.8 s^{-1}) and activated (20.0 s^{-1}) R_2^* in the brain (-0.8 s^{-1}). These signals are referred to as S_{rest} (resting signal) and S_{active} (active signal) [31].	22
Figure 3.5	An illustration of a vessel orientation in a voxel.	23
Figure 3.6	Pulse sequence diagram of DW-EPI.	25
Figure 3.7	Tagging and control techniques in ASL sequence, FAIR. From left to right, non-slice selective inversion experiment, slice selective inversion experiment, difference or perfusion image.	26
Figure 3.8	The absorption spectrum of chromophores.	27
Figure 3.9	Model of optical neuroimaging. Light source in the NIR spectrum emits onto the scalp, detector sensitive to NIR spectrum detects photons as they exit the head [46].	28
Figure 3.10	Absorption spectrum for pure water over the range 650-1050 nm [48].)	29
Figure 3.11	Absorption spectrum for HbO and HbR. Values taken from Cope et al. (1991) [48].	30
Figure 3.12	The propagation of light through a homogeneous medium that is highly scattering. There are some photons being detected due to the scatterin while others are absorbed.	32
Figure 3.13	An illustration of the relative spatial and temporal sensitivities of different functional brain mapping methods that can be used in animals, man, or isolated tissue preparations [60].	36
Figure 4.1	The events that generates BOLD signal [14].	39
Figure 4.2	An illustration of BOLD response which indicates three transients, initial dip, postive BOLD and post stimulus undershoot.	40
Figure 4.3	(a) CBV based intial dip (b) CMRO ₂ based initial dip.	40
Figure 4.4	An illustration of postive BOLD transient. CBF increase exceed the demands of CMRO ₂ . This couses sudden decrease in HbR concentration.	41

- Figure 4.5 An illustration of post stimulus undershoot due to (a) delayed return of CBV (b) CBF undershoot below the baseline (c) continuation of CMRO₂ with respect CBF termination. 43
- Figure 4.6 The balloon model [1]. It is assumed in the model that the vascular bed (CBV) within a small volume of tissue can be modeled as an expandable venous compartment (a balloon) that is fed by the output of the capillary bed. V is the volume of the balloon, F_{in} is the inflow, and F_{out} is the outflow from the balloon. 44
- Figure 4.7 Different balloon model simulation based on (a) linear volume changes of the power law, $CBF = CBV^\alpha$, (b) on modified nonlinear volume changes for the viscoelastic effects, $f_{out}(v, t) = v^{\frac{1}{\alpha}} + \tau \frac{dv}{dt}$. The volume change in this example is to illustrate the type of transients that can arise. BOLD signal shows an initial overshoot, followed by a slight return to a plateau and ending with a strong post stimulus undershoot. Model parameters in these simulations are: for (a) $\alpha = 0.38$, $E_0 = 0.4$, $V_0 = 0.02$, $\tau_0 = 3$, for (b) $\alpha = 0.38$, $E_0 = 0.4$, $V_0 = 0.02$, $\tau_0 = 3$, $\tau = 20$. 47
- Figure 4.8 The effect of alteration in PaCO₂ in animals on the CBF. Zero reference line for CBF is PaCO₂ of 40 mmHg [110]. 49
- Figure 5.1 Diagram of the proposed model linking the applied BHT to the resulting physiological responses and the measured BOLD response. PaCO₂ was used as a driving function of the balloon model instead of CMRO₂ and CBF. 53
- Figure 5.2 Experimental protocol with 4 repetitions of 90 second normal breathing followed by 30 second BHT. 54
- Figure 5.3 Display of selected pixels within ROI in frontal cortex on three sequential axial slices (Subject OS). 57
- Figure 5.4 Averaged time course of BOLD signal of all four subjects. The shaded area represents the time during which the subjects performed the BHT. 58

- Figure 5.5 Changes in cerebral HbO, HbR and tHb obtained by fNIRS for each of four volunteers. Error bars indicate standard deviation. The shaded area represents the time during which the subjects performed the BHT. 59
- Figure 5.6 (a) Average time course of fNIRS derived HbR data and balloon model outputs for q (identical to HbR), f_{in} (identical to CBF) and v (identical to CBV). Shaded areas represent the post stimulus undershoot duration. (b) average time course of BOLD signal measured from fMRI and derived balloon model BOLD signal. Model parameters were $\alpha = 0.38$, $V_0 = 0.02$, $\tau_0 = 3$ s, $\tau_+ = 0$, $\tau_- = 13$, $E_0 = 0.1$. 61
- Figure 5.7 Cerebral blood flow (CBF) as a function of PaCO₂. Graphs obtained from the best fit parameters (Table 5.3) of the Eq. 5.1 used in Figure 5.6. 62
- Figure 6.1 The relationship of BOLD signal change on the baseline level of PaCO₂. Individual data point indicates different subject. 65

LIST OF TABLES

Table 3.1	Magnetic susceptibility values [27].	18
Table 3.2	Thickness and Optical properties (NIR range) of Tissue in Adult Head [52, 51].	32
Table 5.1	Numerical data obtained from simultaneous fNIRS measurements. Averaged HbO and HbR during VMR transient 1 (During 10-20th seconds of breath holding) and transient 2 (During 40-50th seconds of breath holding) traces corresponding to one BHT period. Statistical significance of paired t tests ($P < 0.05$) results indicates comparisons between HbR and HbO.	58
Table 5.2	HbR peak times during post stimulus undershoot for all four subjects as measured by fNIRS and derived from individualized balloon models. Peak times are in seconds after the start of the breath hold duration.	60
Table 5.3	Sigmoidal function parameters in Eq. 5.1 which describe relation between CBF and PaCO ₂ (Figure 5.6).	62

LIST OF SYMBOLS

B	Magnetic Field
H	Magnetic Field Strength
μ_0	Magnetic Permeability
χ	Magnetic Susceptibility
Y	Fractional Oxygenation
Hct	Hematocrit
R_2	Relaxation Rate
TE	Echo Time
V	Blood Volume Fraction
I_0	Incident light intensity
I_L	Transmitted light intensity
OD	Optical Density
λ	Wavelength
$\varepsilon(\lambda)$	Absorption coefficient as a function wavelength
C	Concentration
L	Mean free pathlength
$B(\lambda)$	Correction of mean free pathlength with respect to wavelength
q	Deoxy-hemoglobin Concentration
f_{in}	Flow in
f_{out}	Flow out
E	oxygen extraction fraction
$m(t)$	Cerebral metabolic rate of oxygen
τ_0	Mean transit time through the balloon at rest
τ	Viscoelastic coefficient

LIST OF ABBREVIATIONS

fMRI	Functional Magnetic Resonance Imaging
fNIRS	Functional Near Infrared Spectroscopy
CBF	Cerebral Blood Flow
CBV	Cerebral Blood Volume
CMRO ₂	Cerebral Metabolic rate of Oxygen
BOLD	blood oxygen level dependent
HbR	Deoxy-hemoglobin
HbO	Oxy-hemoglobin
tHb	Total Hemoglobin
SE	Spin Echo
GE	Gradient Echo
DW	Diffusion Weighted
EPI	Echo Planar Imaging
ASL	Arterial Spin Label
EEG	Electroencephalography
MEG	Magnetoencephalography
PET	Positron Emission Tomography
BHT	Breath Hold task
CNS	Central Nervous System
PNS	Peripheral Nervous System
CSF	Cerebrospinal Fluid
PaCO ₂	Partial Pressure of Carbon Dioxide

1. Introduction

Neuroimaging techniques provide an insight to the physiological activities that take place in the brain during health and disease. Due to the remote operation, the information they provide are usually challenged with noise, artifacts and poor resolution. Hence, direct access to the underlying physiology and neurobiology is limited. Researchers have been exploiting various techniques to overcome the limitations with the help of integration of imaging modality and theoretical approaches.

The use of multimodal imaging provides access to complimentary information not obtainable by one modality only. In the case of neuroimaging, this study aims to integrate functional near infrared spectroscopy (fNIRS) and functional magnetic resonance imaging (fMRI) to elucidate the brain hemodynamic response. Nevertheless, still this integration of modalities does not provide full understanding of the sequential neurobiological processes that take place. We propose to fill this gap by the help of biophysical model, namely the expanded balloon model, which is an extension of a neurovascular coupling model.

1.1 Motivation and Objectives

The particular aims of this study are to directly assess the contributions of changes in the deoxyhemoglobin (HbR) concentration and cerebral blood volume (CBV) to the blood oxygen level dependent (BOLD) signal during cerebral activation in humans, and to investigate the temporal behavior of the cerebral blood flow (CBF), CBV, and cerebral metabolic rate of oxygen (CMRO₂). Therefore, we fuse and interpret fNIRS and fMRI measurements during a breath hold task (BHT) and model these signals with the help of a biophysical model.

A biophysical model detailing different aspects of the hemodynamic response is an expansion form of balloon model [1, 2]. There are several recent studies com-

paring the hemodynamic response to neuronal activation as measured by fNIRS with fMRI, though only few of the studies so far have explicitly investigated these data by the conventional balloon model [3]. While recent studies have mostly focused on the correlation of the BOLD signal to the changes in the hemoglobin concentrations, new studies are needed to explore the transients of the BOLD signal by incorporating the fNIRS measurements into the balloon model [3].

As far as we know, this is the first study that investigates BOLD signal during BHT using the balloon model in a combined fMRI-fNIRS study. To do this, we expanded the balloon model by adding partial pressure of carbon dioxide (PaCO_2) parameter as a driving function in order to simulate the hypercapnic effect of BHT on the CBF. Here we report that post stimulus undershoot measured by fMRI is dominated by a slow return of CBV which is supported by fNIRS measurements and simulations of the expanded balloon model. We also report that this expanded balloon model could predict the effect of the initial level of vasodilatory agent (PaCO_2 in this study) on CBF, hence on the BOLD signal. The results are particularly interesting because of their implications for combined measurements of fNIRS and fMRI.

1.2 Outline of the Thesis

This dissertation is organized in the following manner.

Chapter 2 contains a description of the anatomy and physiology of the human brain in general and provides descriptions of the cerebral energy metabolism and its coupling to cerebral blood flow.

Chapter 3 starts with detailed description of primary imaging modalities used in this research, namely fMRI and fNIRS. Then, it compares the different imaging modalities used in functional brain imaging and then focuses on multimodality approaches in the field of Neuroimaging.

Chapter 4 starts with detailed description of underlying physiology of BOLD signal and its constituent transients such as initial dip, positive BOLD and post stimulus undershoot. Hypothesis that try to define these transients are also discussed in this chapter. Then, Balloon model which investigates BOLD signal with dynamics of the intrinsic variables: the flow-inducing signal, the CBF, the CBV and the HbR introduced.

Chapter 5 outlines the fNIRS and fMRI experiments that were conducted during the course of this dissertation research. The results are presented here.

Chapter 6 discusses the results of the proposed method in two aspects: (1) effects of breath hold on cerebral hemodynamics and (2) effects of breath hold on BOLD and fNIRs vasoreactivity transients.

Chapter 7 provides summary of the dissertation research. It summarizes the specific achievements of this research work and provides suggestions for future development and directions for this research.

2. Physiological Background

2.1 Brain Anatomy

The human nervous system consists of the central nervous system (CNS) and peripheral nervous system (PNS). CNS is composed of brain and the associated nerve or spinal cord whereas PNS is composed of nerves extending to and from the brain and spinal cord, respectively. CNS is a very large interactive processor capable of processing a great variety of sensory inputs, of storing information for short or long periods, and of expressing the mental output by language, mimicry or behavior.

Brain is supported and protected by the surrounding skin, skull, meninges and cerebrospinal fluid (CSF) (Figure 2.1). The skin consists of an outer, protective layer, the epidermis and an inner layer, the dermis. The subcutaneous tissue lies deep to the dermis. It is highly vascular and has many nerve endings and contains fat tissue. Skull, protective bony case, holds the brain. Between the bone and the cerebral tissue, there are three layers of membranes, called meninges. Their functions are to protect the CNS and blood vessels, enclose the venous sinuses, retain CSF, and form partitions within the skull. These membranes are dura matter, arachnoid membrane and pia matter. CSF is a salty solution that is continuously secreted by the choroid plexuses and flows into the subarachnoid space between pia matter and the arachnoid membrane. The prime purpose of the CSF is to support and cushion the brain and help nourish it (Figure 2.1).

2.1.1 Major Regions of The Brain and Their Functions

The human brain can be grossly divided into brain stem, cerebellum and the cerebrum (Figure 2.2).

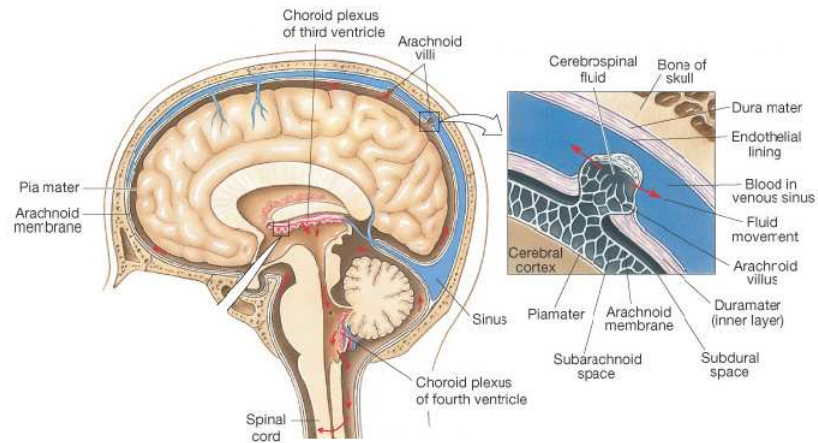


Figure 2.1 An illustration of skin, skull, meninges and CSF [4].

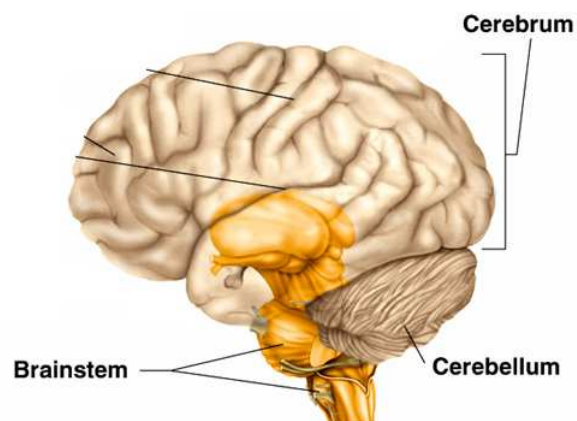


Figure 2.2 Major parts of the brain - cerebrum, cerebellum, brainstem [4].

The cerebrum is divided into two hemispheres, the left and the right, separated by the longitudinal fissure. Anatomically these are identical in form, each being split into four lobes; the frontal lobe, the parietal lobe on the top, the temporal lobe on the side, and the occipital lobe at the back. The cerebral cortex constitutes a 2-4 mm thick grey matter in the surface layer. It consists of nerve cell bodies, dendrites and axon terminals. It is responsible for conscious behaviour and contains three different functional areas: the motor areas, sensory areas and association areas. Located internally are the white matter which consists of mostly axons and is responsible for communication between cerebral areas and between the cerebral cortex and lower regions of the CNS.

Brain stem is an extension of the spinal cord and consists of grey matter surrounded by white matter fibre tracts. It is divided into three main sections: the medulla oblongata, the pons, and the midbrain. The medulla oblongata takes an important role as an autonomic reflex centre involved in maintaining body homeostasis. The pons act as a relay station for information transfer between cerebellum and cerebrum and it also coordinates the control of breathing along with the medulla. The midbrain controls the eye movement, but it also relays signals for auditory and visual reflexes. The cerebellum is located dorsal to the pons and medulla. The cerebellum processes impulses received from the cerebral motor cortex, various brain stem nuclei and sensory receptors in order to appropriately control skeletal muscle contraction, thus giving smooth, coordinated movements.

2.1.2 Functional Organization of The Brain

The detailed functional organization of much of the brain is poorly understood. However many of the regions involved in sensory, motor and association function have been identified.

The primary visual cortex is located in the occipital lobe, which deals with the reception and interpretation of vision. Auditory inputs are interpreted on the opposite side of the brain to the ears. The primary auditory cortex is located in

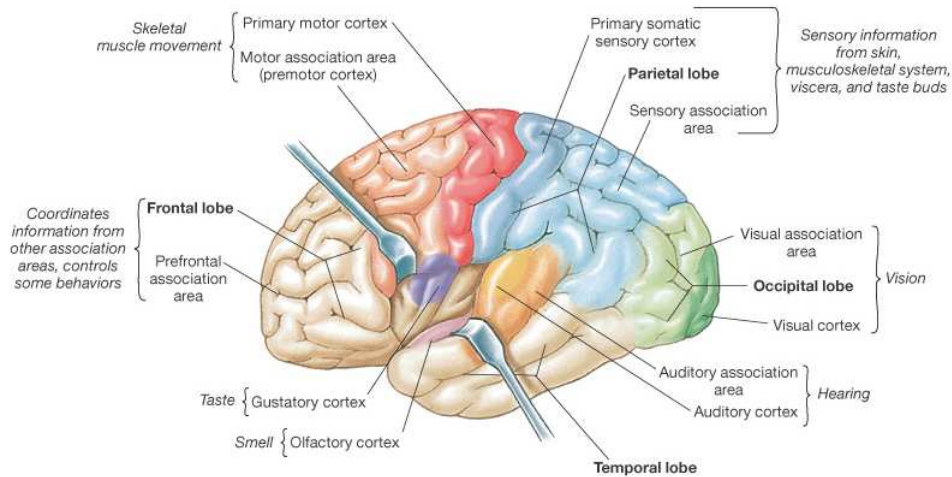


Figure 2.3 Functional areas of cerebral cortex [4].

the temporal lobe, with the right ear mapping on to the left hemisphere, and vice-versa. Similarly signals from the many touch receptors over the body end up in the somatosensory cortex, which is located in the parietal lobe, just behind the central sulcus. The sensations of taste and smell are mediated by the gustatory and olfactory systems. The olfactory bulb is located on the inferior surface of the frontal lobe, whereas the gustatory cortex is in the temporal lobe. The motor areas, in the frontal lobe process information about skeletal muscle movement and play a key role in voluntary movements. Association areas integrate sensory information such as somatic, visual and auditory into perception (Figure 2.3).

2.1.3 Cellular Architecture of The Brain

Neurons are the cell type of the brain which carry and generate electrical signals in the brain. They have a very important and complex task, which would be impossible to accomplish alone. There are specialized cells whose main function is to support neurons, and neural activity. These smaller cells surround and wrap or support and protect the delicate neurons. These are collectively called neuroglia or glial cells. Glial cells were first thought of as merely “nerve glue” which kept neurons together. It is now known that each glial cell type has its own function: microglia are the macrophages of the brain, that become activated during inflammation, Schwann cells and oligoden-

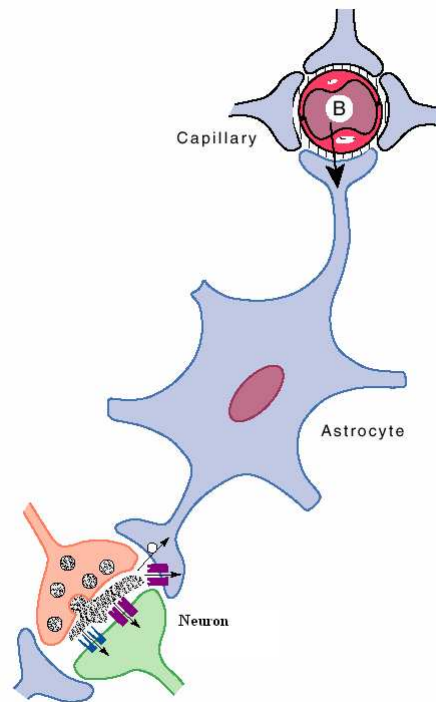


Figure 2.4 Schematic representation of cytological relations existing among capillaries, astrocytes and neurons [5].

drocytes sheath the axons and cell bodies in the periphery and central nervous system respectively, for support and increased conductivity. Finally, astroglia are star-shaped glial cells, which form an intervening layer between the neurons and the blood vessels. Therefore, capillaries and neurons are indirect contact (Figure 2.4). Due to this, it was suggested that astrocytes could play a role in cerebral energy metabolism.

2.2 Brain Energy Metabolism

Although the human brain only weighs 2-3 % of the total body weight, it may consume up to 25 % of the body's energy supply [6]. Glucose is the primary energy substrate of the brain. In cerebral energy metabolism, one glucose molecule and six oxygen molecules ultimately lead to carbon dioxide and water. In this oxidative process, mainly in the citric acid cycle, energy is created from glucose in the form of 36 molecules of ATP (Figure 2.5) [4]. Energy formation can also be anaerobic, in which glucose is degraded to lactate without oxygen. This process is less efficient, as it only produces

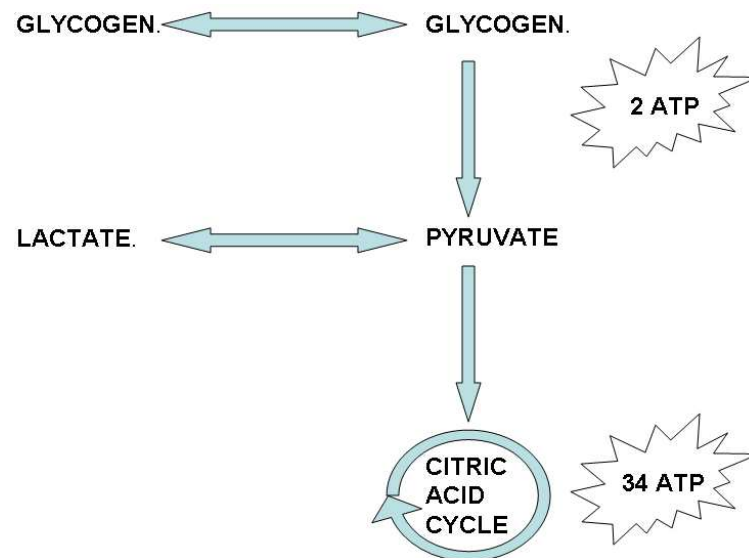


Figure 2.5 The Glucose metabolism. Glucose can be derived from glycogen. Through glycolysis, glucose is transformed into pyruvate, which yields 2 ATP. Lactate is anaerobically formed from pyruvate. With oxygen, pyruvate is metabolized in the citric acid cycle, which yields another 34 ATP.

2 ATP per glucose [4]. Conventionally it is thought that lactate is formed only in emergency situations (e.g. hypoxia). The current view is that lactate is formed during most neuronal activation, without apparent oxygen deficiency [7].

The main energy-consuming process of the brain is the maintenance of ionic gradients across the plasma membrane, a condition that is crucial for excitability. Maintenance of these gradients is achieved predominantly through the activity of ionic pumps fueled by ATP, particularly Na^+ , K^+ -ATPase, localized in neurons as well as in other cell types such as glia. Activity of these pumps accounts for approximately 50% of basal glucose oxidation in the nervous system [8]. As in other tissues, the metabolism of glucose, the main energy substrate of the brain, produces in the form of energy: ATP. Glycolysis and the citric acid cycle produce ATP. Maintenance of the electrochemical gradients is the main energy-consuming process of neural cells, particularly for Na^+ and K^+ .

Astrocytes surround brain capillaries. This implies that glucose, taken up by the brain, first enters the astrocytic end feet instead of the extracellular space (Figure 2.6). The neuron is thus, both functionally and anatomically, downstream of the astrocyte, and may get energetic substrates from the blood via the astrocytes. The question

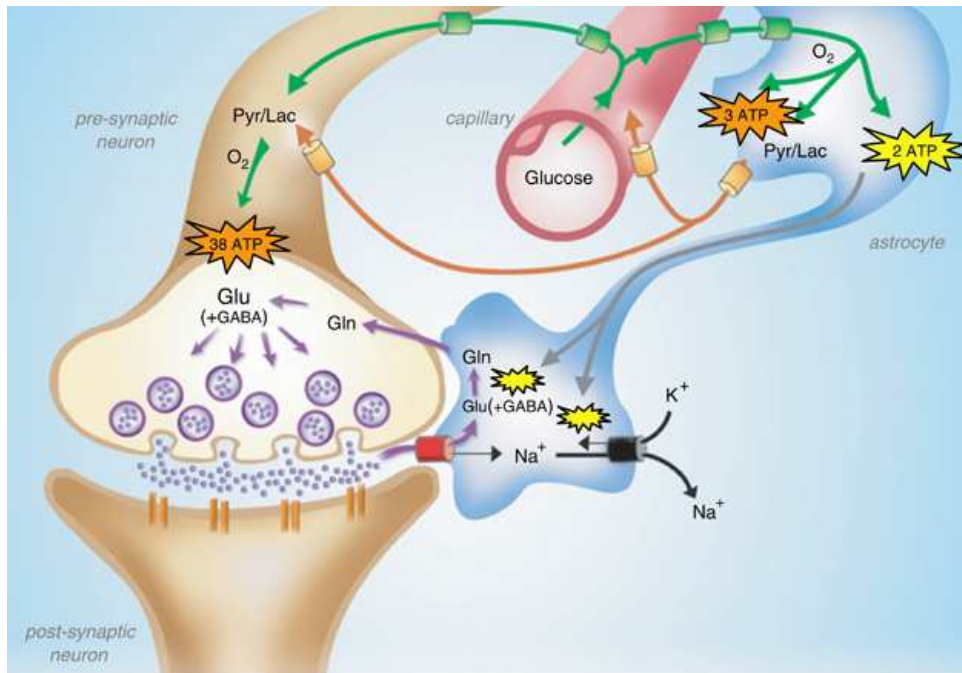


Figure 2.6 An illustration of astrocyte-neuron lactate shuttle [5].

has been arisen whether the function of astrocytes is limited to glucose uptake and distribution to neurons, or whether astrocytes release a metabolic intermediate of glucose. Up to now, it is only possible to model the in vivo metabolism for simpler neural systems such as the retina, or in vitro preparations of neurons and glia [9, 10, 11, 12]. With these neurovascular models, various evidences are found suggesting the release of lactate as an intermediate substrate by astrocytes [13]. For example, astrocytes release large amounts of lactate, which is stimulated by neurotransmitters, and neurons may use lactate as an energy source. Based on this evidence, the hypothesis was raised for the astrocyte-neuron lactate shuttle, in which lactate, released by astrocytes, is proposed as the metabolic neuronal substrate during neuronal activity (Figure 2.6) [13]. In response to neuronal activation at glutamatergic synapses, astrocytes increase glucose use and lactate production, despite sufficient oxygen levels to support complete aerobic metabolism [5]. The astrocytically produced lactate is released into the extracellular space, from where it is taken up and aerobically metabolized by neurons during activity (Figure 2.6).

2.2.1 Coupling of Brain Energy Metabolism to Blood Flow

As cerebral metabolic activities need more energy, in the form of glycogen, it is supported by the cerebral blood flow (CBF, approximately 12% of cardiac output [6]). CBF serves both to deliver glucose and oxygen, the metabolic substrates that fuel the brain, and to carry away the waste products of metabolism, carbon dioxide and heat [14]. For this reason it is not surprising that focal increases in CBF closely follow neural activity. Thus, the CBF is supposed to be dynamically and precisely adjusted to metabolism, thereby reflecting underlying neuronal activity [15, 16, 17, 18].

Flow in capillaries is controlled by the smooth muscle surrounding vessel. The smooth muscle constricts and dilates on the basis of alterations in the concentrations local metabolites which are called vasodilatory agents. Based on this concept, two mechanisms may control these blood flow: the first one is related to energy use; the second one is based on neural signaling to the local vasculature. As stated before, changes in the concentrations of local metabolites may lead to changes in regional CBF. Several chemical substances capable of cerebral autoregulation during the neuronal activity have been considered as mediators of the coupling between CBF and metabolism. Metabolic factors are currently thought to be vasodilatory agents in cerebral autoregulation include concentrations of adenosine, positively charged ions (H^+ , K^+) and blood gasses (CO_2 and O_2).

2.2.1.1 Adenosine and Positively Charged Ions. K^+ , represents a potential vasodilatory agent associated more directly with neuronal activity, in particular with action potentials. Increased neuronal activity, as seen in a higher frequency of action potential, leads to the release of K^+ into the extracellular space [19]. Therefore intra/extracerebral K^+ concentration gradient become high. This rise in K^+ concentration in extracerebral space causes dilatation of the brain arterioles (Figure 2.7).

After the neuronal activity, ion distribution of extra/intracerebral space should be reestablished on a long term basis. Thus, Na^+K^+ pump is activated to re-establish

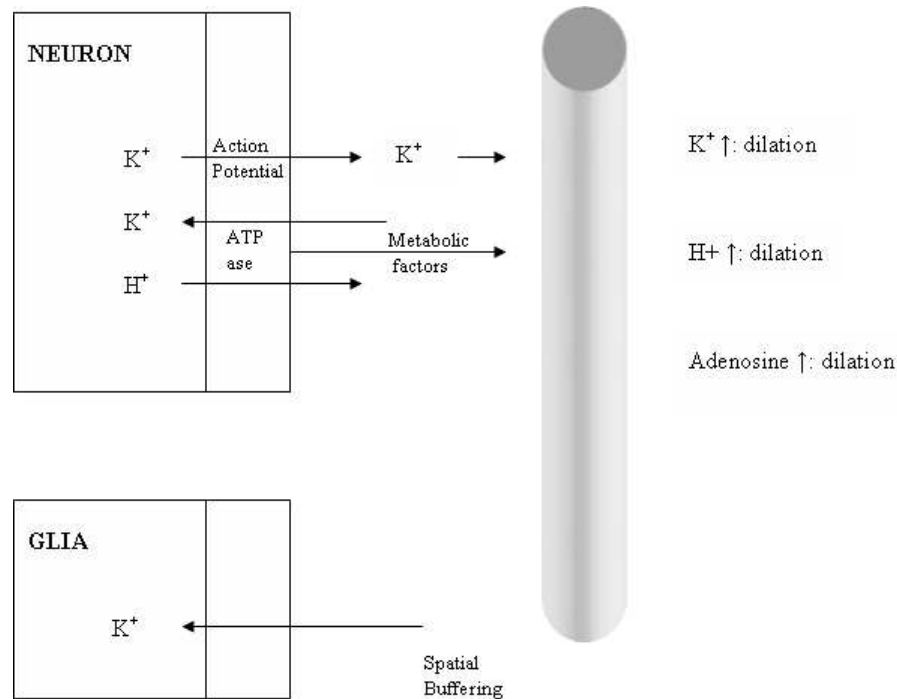


Figure 2.7 Dynamic components of coupling between functional activity, metabolism and blood flow in the brain. The activity dependent element is represented by K^+ , the metabolic element by H^+ and adenosine [19].

the intra/extra-cellular ion distribution by carrying K^+ back into and Na^+ out of the cells. Increased activity of Na^+K^+ pump is fueled by metabolic energy. Following metabolic activity (stated in the previous subsection), H^+ and adenosine are released due to the Na^+K^+ pump into the extracerebral space. In addition to K^+ , H^+ and adenosine have been identified as vasodilatory activity which controls to local CBF following a neuronal activity (Figure 2.7). This neurovascular coupling is the basis for neuroimaging methods which make use of metabolic activity as an indicator of function. Hence it is fair to assume that neuronal activity is directly coupled to CBF.

2.2.2 Blood Gases and Cerebral Blood Flow

Although the human brain is 2% of the body's weight, it accounts for 20% of its resting metabolism [8, 20]. Neuronal activity in the brain depends on the continuous and adequate supply of oxygen. Thus nearly 20% of the oxygen taken up by the whole body at rest is utilized by the brain [4]. However, the effects of partial pressure

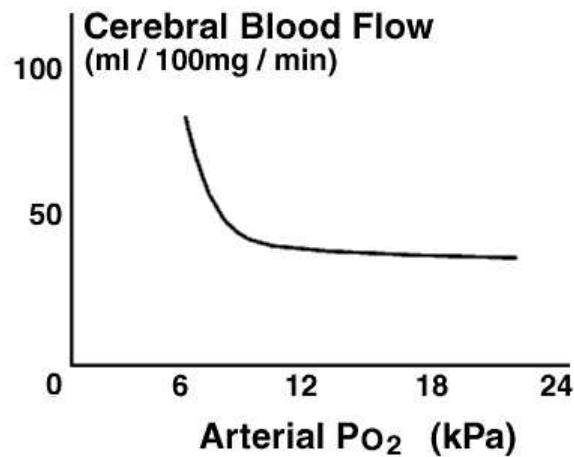


Figure 2.8 The response of cerebral circulation to changes in arterial oxygen tension [21].

of O_2 (PaO_2) are not as marked as CO_2 changes. Moderate variations of O_2 above and below the normal level do not affect CBF. Low arterial oxygen tension also has profound effects on CBF (Figure 2.8). A decrease in PaO_2 during hypoxia reliably increase cerebral perfusion by decreasing cerebrovascular resistance as a result of arterial vasodilation. Conversely, an increase in PaO_2 (hyperoxia) result in a decrease in CBF (Figure 2.8). When it falls below 50 mmHg (6.7 kPa), there is a rapid increase in CBF and arterial blood volume.

The continuation of a sufficient blood to the brain implies a relation between the flow rate to the cerebral metabolism. A significant amount of oxygen is utilized for oxidative phosphorylation on a continuing basis by brain tissue, and CO_2 , the principal end-product of aerobic metabolism, must be constantly removed. CO_2 and O_2 readily diffuse across the microvessels wall. Thus, their tensions (partial pressures) in the blood in cerebral microvessels and in surrounding tissues tend to be in equilibrium under normal physiological conditions. The relationships between the O_2 and CO_2 contents of arterial blood and CBF have been extensively investigated, and they will be briefly discussed here.

In the normal brain, the constancy of CBF and CBV relies upon the intrinsic ability of the cerebral resistance vessels to alter their diameter in response to variations in blood pressure (CBF autoregulation) and changes in metabolic demands [22]. One

of the major products of increased cerebral metabolic activity is a decrease in O_2 and concomitant increase in CO_2 . About 8% of the CO_2 in the blood is dissolved in the plasma. 20% is bound to hemoglobin. 72% diffuses into the red blood cell where carbonic anhydrase combines it with water to form carbonic acid [4].

CO_2 can alter cerebrovascular resistance and ultimately affect CBF [22]. CO_2 is freely diffusible between arterial blood and brain tissue. Thus it can diffuse into the vascular smooth muscle cell from either brain tissue or the vessel lumen, while hydrogen ions in the vessel lumen are prevented from reaching the smooth muscle cell by the blood-brain barrier [4, 14, 19]. Even though the chemical reaction between CO_2 and tissue water is simple:



The physiologic mechanisms that underlie the responses of the cerebral vessels to changes in CO_2 have not been simple to ascertain. The main mechanism of this effect upon cerebral vessels appears to be perivascular pH [23, 24], but there may be additional unknown mechanisms. It was suggested that the action of CO_2 was mediated by direct effect of H^+ on cerebrovascular smooth muscles [25]. In this study, CO_2 was applied directly and externally to the cerebral cortex resulting in vasodilation. This strongly suggested the vasodilatory action of extravascular CO_2 , a product of cerebral metabolism. According to this, an increase in CO_2 in the plasma, result in CO_2 crossing blood brain barrier. There, CO_2 react with H_2O to make bicarbonate ion and hydrogen ion. An increase in the level of hydrogen ion causes pH to decrease. All this activities lead to the conclusion that CO_2 vasomotor activity is the change of intracellular H^+ in arteriole smooth muscle (Figure 2.9).

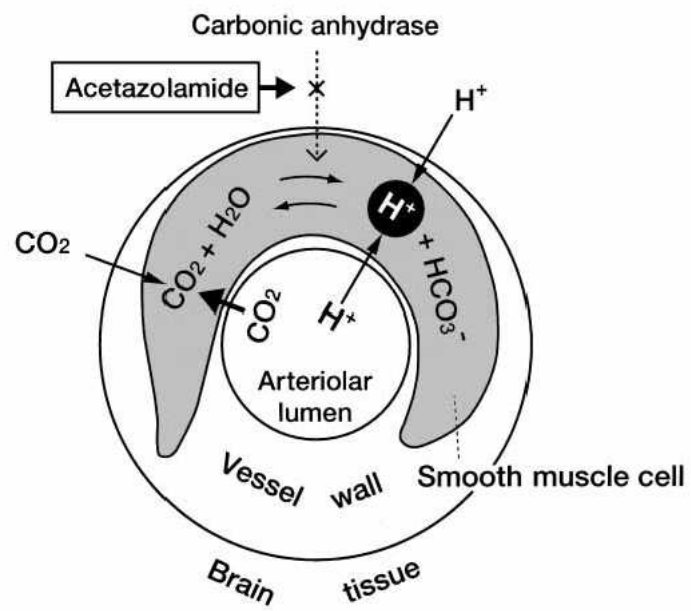


Figure 2.9 Cerebral vasodilator activity of CO₂ [26].

3. Neuroimaging Techniques

This section consists of physical background of functional magnetic resonance imaging (fMRI) and functional near infrared spectroscopy (fNIRS) and review of other neuroimaging modalities.

3.1 Functional Magnetic Resonance Imaging

MRI is based on the nuclear magnetic resonance of hydrogen atoms (protons) in water. When protons are placed in a strong magnetic field and exposed to a pulse of radio waves of a particular frequency, they resonate or emit energy of the same frequency. The resonance signal can be spatially localized by applying magnetic-field gradients in three dimensions and the localized signals can be converted to an anatomical image. Because the signal contains information about whether the hydrogen atoms are present as free water or are partially bound in molecular structures such as white matter, gray matter. MRI can differentiate various tissue types (Figure 3.1). This information comes from intrinsic parameters of tissue, including the nuclear spin density (proton density), the spin-lattice relaxation time T_1 and the spin-spin relaxation time T_2 . Thus it reveals excellent anatomical detail, particularly of soft tissues. fMRI, in contrast, monitors changes in local brain activity by measuring signals that depend on the differential magnetic properties of HbR and oxy-hemoglobin (HbO), termed the BOLD signal.

Substances can be classified according to their magnetic susceptibilities which is the ability of a substance to produce an internal magnetic field in response to an applied magnetic field. Therefore, magnetic field strength depends on the material property of magnetic susceptibility:

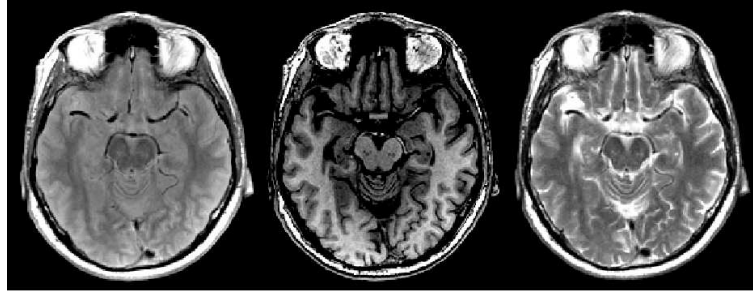


Figure 3.1 Cross sectional brain image. From left to right: proton density weighted, T₁ weighted, T₂ weighted images.

$$B = \mu_0(H + \chi H) \quad (3.1)$$

where μ_0 is magnetic permeability, χ is magnetic susceptibility, H is the magnetic field strength and B is the magnetic field. χ can be positive or negative: paramagnetic ($\chi > 0$) and diamagnetic ($\chi < 0$). In paramagnetic materials, there are permanent magnetic moments and when they are placed in an external field; its atomic moments tend to line up with field. On the other hand, when a magnetic field applied to the diamagnetic materials, a weak magnetic moment is induced in the direction opposite the applied field.

As in fMRI, much of the iron in the blood is in the hemoglobin, or more specifically in one of two states, deoxy-hemoglobin (HbR) or oxy-hemoglobin (HbO) (Figure 3.2). HbR is paramagnetic and when oxygen binds to hemoglobin, it becomes HbO, paramagnetic effect is reduced (Table 3.1). The result is that the magnetic susceptibility of blood varies linearly with blood oxygenation [27].

The magnetic susceptibility of blood is affected by the level of oxygenation (Y , fractional oxygenation) can written as follows:

$$\chi_{blood} = Hct(Y\chi_{oxy} + (1 - Y)\chi_{deoxy}) + (1 - Hct)\chi_{plasma} \quad (3.2)$$

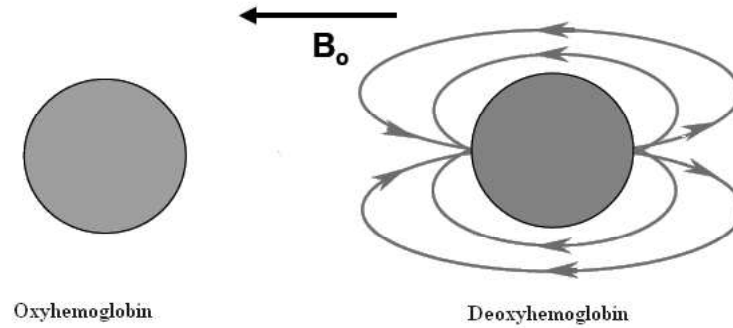


Figure 3.2 Magnetic field distortion due to paramagnetic HbR and diamagnetic HbO. There is no distortion around HbO. However, There is a dipole field distortion in surrounding of HbR.

Table 3.1
Magnetic susceptibility values [27].

Type of Magnetic Susceptibility (χ)	Material	Magnetic Susceptibility
Diamagnetic	Water (37)	-9.05×10^{-6}
	Human Tissues	-11.0×10^{-6} to -7.0×10^{-6}
	Cortical Bone	-13×10^{-6} to -9.0×10^{-6}
	Whole Blood (deoxygenated))	-7.9×10^{-6}
	Red Blood Cell (deoxygenated))	-6.52×10^{-6}
Paramagnetic	Hemoglobin Molecule (deoxygenated))	0.15×10^{-6}

where Hct is the hematocrit (fraction of blood volume occupied by red blood cells). We assume that $\chi_{oxy} = \chi_{plasma} = \chi_{tissue} = \chi_{water} = 0$. Then, Eq. 3.2 is reduced to:

$$\chi_{blood} = Hct((1 - Y)\chi_{deoxy}) \quad (3.3)$$

A change in oxygenation will result in a change in the susceptibility of blood:

$$\Delta\chi_{blood} = \Delta Y Hct \chi_{deoxy} \quad (3.4)$$

The physical basis of the BOLD sensitivity of MR signal is that HbR alters the magnetic susceptibility of blood. During brain activation, due to the paramagnetic properties of HbR, it creates magnetic field gradient which shortens T_2 (free relaxation, Eq. 3.5), T_2^* (free induction decay) (also termed as R_2 and R_2^* respectively) and reduces MR signal [28, 29, 27, 30]. However, brain activation leads to a much larger increase in blood flow than oxygen metabolism so the net O_2 extraction fraction drops with activation and then the capillary and venous blood are more oxygenated. This means that there is less Hb present in the voxel. T_2^* becomes longer and the signal measured with T_2 and T_2^* weighted pulse sequence increases.

$$R_2^* = R_2 + R_2' \quad (3.5)$$

Now, we look at the R_2' term, as this is the one that is most relevant to fMRI. An approximate relationship between this and blood properties is:

$$R_2' = \gamma B_0 V Hct (1 - Y) \chi_{deoxy} \quad (3.6)$$

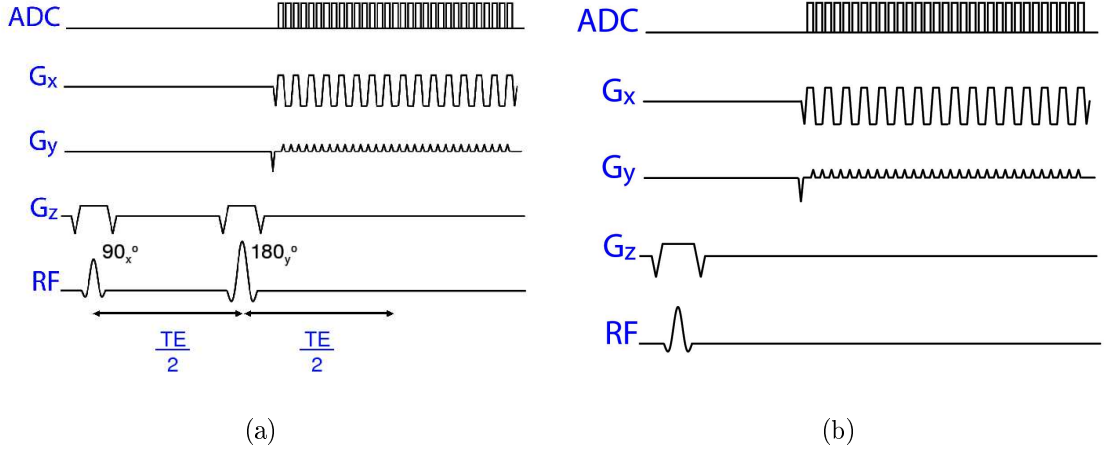


Figure 3.3 fMRI pulse sequences. (a) SE-EPI sequence. Spin echo formed by the 90-180 pulse pair at the center of the EPI readout period, which ordinarily is the center of k-space. (b) GE-EPI sequence. In this sequence, EPI readout period follows a single radiofrequency pulse, whose flip angle is 90.

where V is the blood volume fraction, Y is the fractional oxygenation, $Hct(1 - Y)$ is the total amount of HbR, $B_0\chi_{deoxy}$ is the size of magnetic field perturbation and γ is gyromagnetic ratio.

Thus, we have the decay rate, R'_2 being related to the total amount of HbR and V .

$$R'_2 \propto V[HbR] \quad (3.7)$$

In order to link these expressions to common used BOLD-fMRI sequences, Spin Echo-Echo Planar Imaging (SE-EPI, Figure 3.3(a)) and Gradient Echo-Echo Planar Imaging (GE-EPI, Figure 3.3(b)), following models can be used for MR signal [31]:

For SE-EPI signal

$$S(T_E, T_R) = S_0(1 - 2e^{-(T_R - T_E/2)/T_1} + e^{-T_R/T_1})e^{-T_E/T_2} \quad (3.8)$$

and GE-EPI signal

$$S(T_E, T_R, \theta) = S_0 e^{-T_E/T_2^*} \frac{(1 - e^{-T_R/T_1} \sin\theta)}{1 - e^{-T_R/T_1} e^{-T_R/T_2^*} - (e^{-T_R/T_1} - e^{-T_R/T_2^*}) \cos\theta} \quad (3.9)$$

where T_E and T_R are echo and repetition time respectively. For long T_R ($T_R \gg T_1$) and θ approaches to 0 (small flip angle), these equations reduce to

SE signal

$$S(T_E) = S_0 e^{-T_E R_2} \quad (3.10)$$

GE signal

$$S(T_E) = S_0 e^{-T_E R_2^*} \quad (3.11)$$

According to these models, It is well known that when neural activity increases in a region of the brain, the local MR signal produced in the part of the brain increases by a small amount due to the changes in blood oxygenation so does the local susceptibility. Contrast between two signal intensities (S_{active} and S_{rest}), having a difference in relaxation rate equal to ΔR_2^* , can be approximated as follows (Figure 3.4):

$$\Delta S = S_{active} - S_{rest} = S_0 e^{-R_{2active}^* TE} - S_0 e^{-R_{2rest}^* TE} \quad (3.12)$$

$$\Delta S = S_0 e^{-(R_{2rest}^* + \Delta R_2^*) TE} - S_0 e^{-R_{2rest}^* TE} = S_0 e^{-R_{2rest}^* TE} (e^{-\Delta R_2^* TE} - 1) \quad (3.13)$$

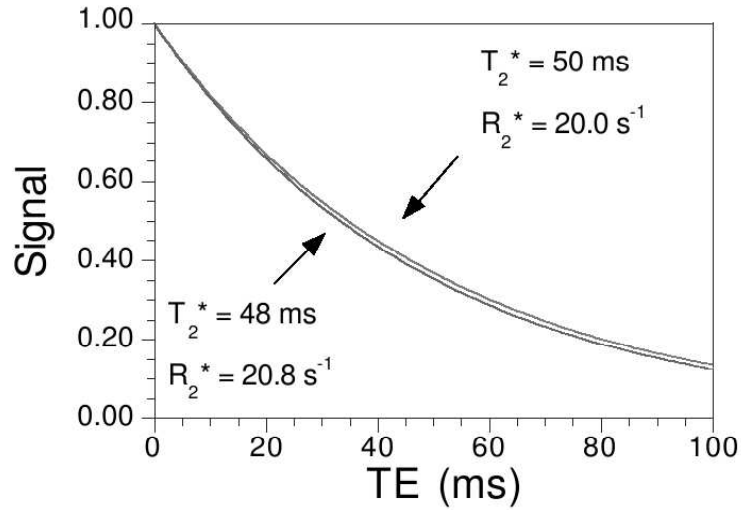


Figure 3.4 Plot of Signal vs. TE, using Eq. 3.11, S_o equals to 1. The two curves represent typical values of R_2^* in the brain. The difference in relaxation rates represent typical differences between resting (20.8 s^{-1}) and activated (20.0 s^{-1}) R_2^* in the brain (-0.8 s^{-1}). These signals are referred to as S_{rest} (resting signal) and S_{active} (active signal) [31].

where R_{2rest}^* is the relaxation rate associated with a measured S_{rest} at a given TE value. For small signal change, the measured fractional (or percentage) signal change is then

$$\frac{S_{active} - S_{rest}}{S_{rest}} = (e^{-\Delta R_2^* TE} - 1) \quad (3.14)$$

$$\simeq -TE \Delta R_2^* \quad (3.15)$$

$$\simeq -TE \gamma B_0 V Hct (1 - Y) \chi_{deoxy} \quad (3.16)$$

This approximation is the basis for BOLD effect (Figure 3.4).

In the last decade, fMRI has been widely used to map change in the brain hemodynamics produced by cognitive tasks. However, due to its signal acquisitions, it has some uncertainties. It is generally believed that significant portion of these signal arises from large veins with additionally contribution from capillaries and parenchyma. CBV, CBF and $CMRO_2$ have different effects on BOLD signal [32, 2]. These large veins and physiological activities give rise to uncertainty in localization of fMRI signals

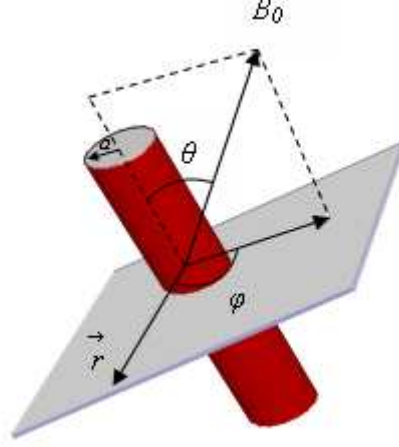


Figure 3.5 An illustration of a vessel orientation in a voxel.

and make it difficult to understand the underlying physiology. In order to suppress and eliminate these uncertainties, several methods have been proposed. Diffusion weighted (DW) EPI [33, 34, 35, 36, 37] and Arterial Spin Label (ASL) [38, 39, 40, 41, 42] offers more accurate information about site of activities and also signal changes.

3.1.1 DW-EPI

It has been previously established that BOLD signal can be modelled according to small oriented vessel (Figure 3.5) [43]. So that signal changes are observed from both intravascular (in the cylinder) and extra vascular (surrounding) space due to magnetic field or frequency difference. When we formulize this scenario with respect to Figure 3.5, the spatial dependence of the induced magnetic field, ω , can be defined according to the following equation for $r < a$ (in the cylinder)

$$\omega_{IV} = 2\pi\Delta\chi B_0(1 - Y)(3\cos_2(\theta) - 1)/3 \quad (3.17)$$

and $r \geq a$ (surrounding space)

$$\omega_{EV} = 2\pi\Delta\chi(1 - Y)B_0\sin^2(\theta)\left(\frac{a}{r}\right)^2\cos(2\varphi) \quad (3.18)$$

In the equations above B_0 is the main magnetic field, $(1 - Y)$ degree of deoxygenation of the blood, θ is the angle between B_0 and cylinder axis, a is the cylinder radius, r is the distance between the point of interest and the center of the cylinder cross section in the plane normal to the cylinder, and φ is the angle between r and the component B_0 in the plane.

Due to the symmetry of extravascular magnetic field and $\cos(2\alpha)$ term, phase shift from the extravascular space added to the net phase in imaged voxel is zero. However, phase shift occurred in MR signal is received from the intravascular space. Diffusion-Weighted (DW) acquisitions can be used to extract the phase shift, ψ_{IV} , from the MR signal directly [37, 34, 36, 33].

For an array of randomly oriented vessels with velocity v , bipolar, z directed diffusion gradient profile with G Gcm^{-1} gradients, pulse width δ and time between onset of the pulse equal to Δ will provide significant signal attenuation $kv_t > \pi$, where v_t is a sequence-dependent velocity threshold, and

$$k = 2\pi\gamma \int tGdt \quad (3.19)$$

Any large vessel with plasma velocity spread Δv such that $k\Delta v > \pi$ will be attenuated. The diffusion weighting (b value) for such a sequence is approximately

$$b = (2\pi\gamma G)^2 \delta^2 \left(\Delta - \frac{\delta}{3}\right) \quad (3.20)$$

By using appropriate b values, it is possible to eliminate intravascular components of BOLD signal with DW-EPI(Figure 3.6) [33]. This enhances spatial selectivity and provides a powerfull tool to investigate the sources of functional signal in BOLD-

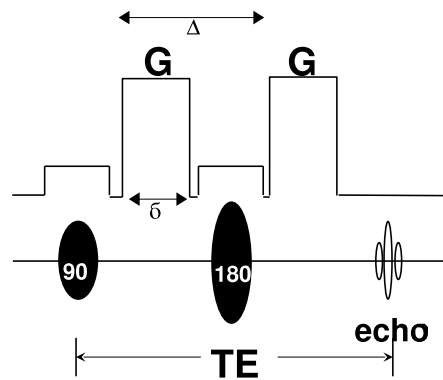


Figure 3.6 Pulse sequence diagram of DW-EPI.

fMRI.

3.1.2 ASL

BOLD signal depends on combination of changes in CBF, CBV and $CMRO_2$. However, qualitative links between these parameters and neural activity are still poorly understood. Hence, it is important to measure CBF, CBV and $CMRO_2$ to understand BOLD phenomena. ASL techniques provide noninvasive images of local CBF with better spatial and temporal resolution. It is not widely available for clinically because ASL is still open area for development and researchs. However, preliminary results showed that ASL could overcome uncertainty of BOLD signal originate from perfusion alterations by a direct measurement of CBF.

In ASL technique, arterial water is used as an endogenous tracer for perfusion measurement. Magnetically tagged arterial water that feeds imaged tissue will have different magnetization state than the tissue. Tagging is typically applied by using RF inversion pulse at a location proximal to the imaged slice. After time of delay, tagged blood is arrived to tissue of interest and exchanged with the water molecules in the tissue which causes MR signal. Tissue of interest is imaged by MR in both case with and without tagging. The difference image can be viewed as a qualitative flow image (Figure 3.7) [44].

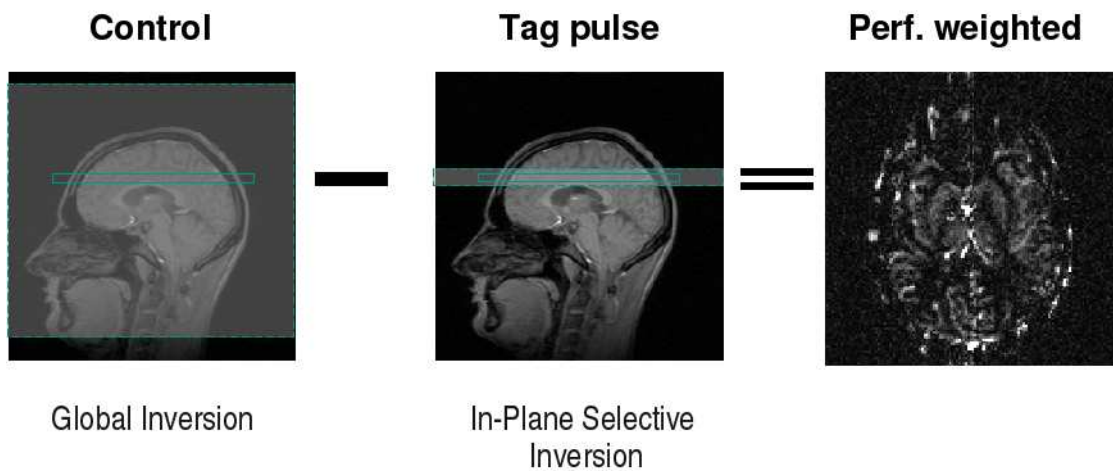


Figure 3.7 Tagging and control techniques in ASL sequence, FAIR. From left to right, non-slice selective inversion experiment, slice selective inversion experiment, difference or perfusion image.

Brain activation imaging by CBF sensitive ASL has several potential advantages over the BOLD. ASL measurements can be used to obtain qualitative or quantitative measurements of CBF change. This provides better localization in the brain tissue.

3.2 fNIRS

Optical neuroimaging is a rapidly developing method which has provided enormous information about the mechanisms of damage in the neonatal brain, and the functional development and process of both the normal and abnormal brain.

3.2.1 Principles of Near-Infrared Spectroscopy

Optical imaging of the human brain is possible because there is a *window* of transparency of biological tissue to light in the near infrared part of the spectrum. Near-infrared (NIR) light from approximately 650-950 nm is even more weakly absorbed by tissue than the red wavelengths. In Figure 3.8, light in the optical window is able to penetrate tissues, so that it can be used to measure hemoglobin concentration in the brain, and deduce CBV [45]. In addition, *HbO* and *HbR* have different absorption characteristics, so that changes in blood oxygenation can be measured. All of the

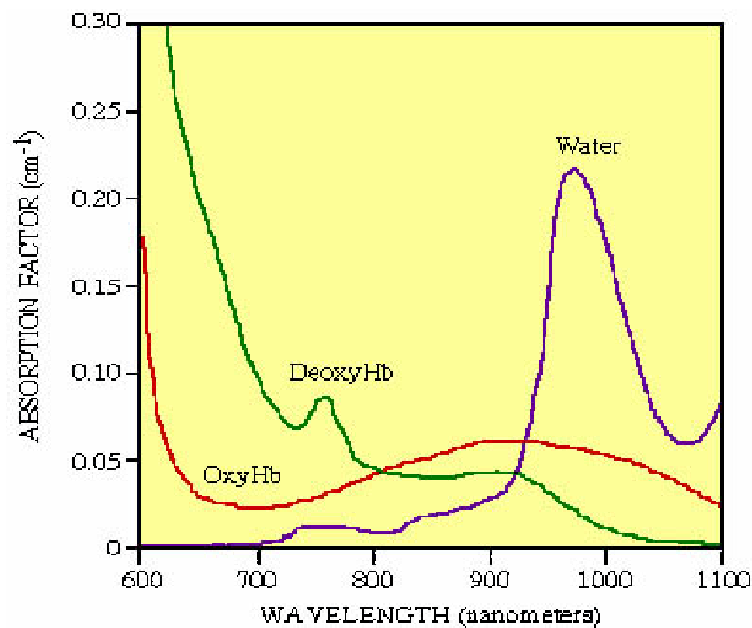


Figure 3.8 The absorption spectrum of chromophores.

optical neuroimaging techniques are based on the same model -shine light onto the scalp, detect it as it exits the head, and use the absorption spectra of the light absorbing molecules (chromophores) present in tissue to interpret the detected light levels as changes in chromophore concentrations (Figure 3.9).

When NIR Light transports in tissue, it gathers information about physiological and morphological changes of tissue as optical properties such as absorption and scattering. Changes are often accompanied by an altered cell metabolism, changes in normal composition of solutes and chromophores, modified DNA and mitochondrial content of the cells, alterations in the shape of cells and organelles. These changes have a characteristic and varied impact on the tissue absorption and scattering properties.

3.2.1.1 Absorption. When the light energy absorbed in tissue, it is most often converted to heat but can also re-emitted as fluorescence or photochemical reaction. Absorbed light is converted to heat or radiated in the form of fluorescence. It is also consumed in photobiochemical reactions. Absorption is wavelength dependent and its spectrum depends on the type of predominant absorption centers and water content of tissues. The absorption of light intensity in a non-scattering medium is described by

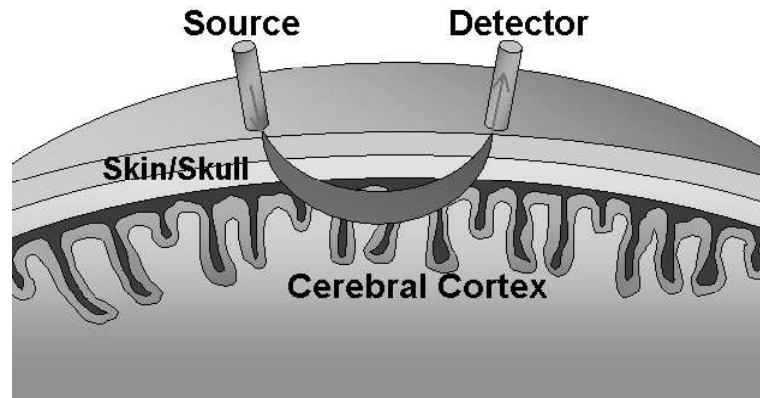


Figure 3.9 Model of optical neuroimaging. Light source in the NIR spectrum emits onto the scalp, detector sensitive to NIR spectrum detects photons as they exit the head [46].

the Beer-Lambert Law. This law states that for an absorbing compound dissolved in a non-absorbing medium:

$$I_L = I_0 e^{-\varepsilon(\lambda)CL} \quad (3.21)$$

where I_0 is the incident light intensity, I_L is the transmitted light intensity through the medium, $\varepsilon(\lambda)$ is the absorption coefficient as a function of wavelength, C the concentration of the absorber, and L is the optical pathlength (distance from source to detector). This equation can be changed to yield direct information on C , the concentration of the absorber, as:

$$OD(\lambda) = \log(I_0/I_L) = \varepsilon(\lambda)CL \quad (3.22)$$

A compound which absorbs light in the spectral region of interest is known as a chromophore. Each chromophore has its own particular absorption spectrum which describes the level of absorption at each wavelength. The principle chromophores in tissue are outlined below:

Water

As shown in Figure 3.10, the absorption of light by water is relatively low be-

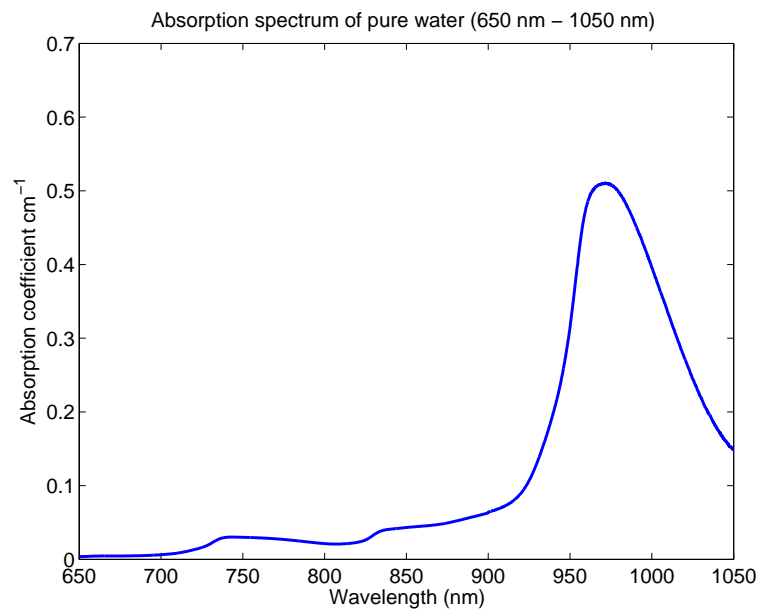


Figure 3.10 Absorption spectrum for pure water over the range 650-1050 nm [48].)

tween 200 - 900 nm. Beyond 900 nm absorption starts to rise with increasing wavelength and peak value is at 970 nm. The high concentration of water in living tissue, typically 80% in adult brain tissue determines the wavelength region in which spectroscopic examination of tissue is possible by strongly limiting the tissue thickness through which light can penetrate. For this reason, the water spectrum is said to demonstrate a "window" of transparency between 200 and 900 nm within which spectroscopic measurements can be made [47].

Lipid

Although the distribution of lipid in tissue is dependent upon tissue type, it can also be thought of as a constant absorber with changes in its concentration throughout the course of a clinical measurement being unlikely. The absorption spectrum of lipid is approximately the same as that of water and it can involve 10-40% of tissue [47].

Melanin

Melanin, found in the epidermis layer of skin, is a highly effective absorber of light, especially in the ultraviolet region of the spectrum. Although this absorption can

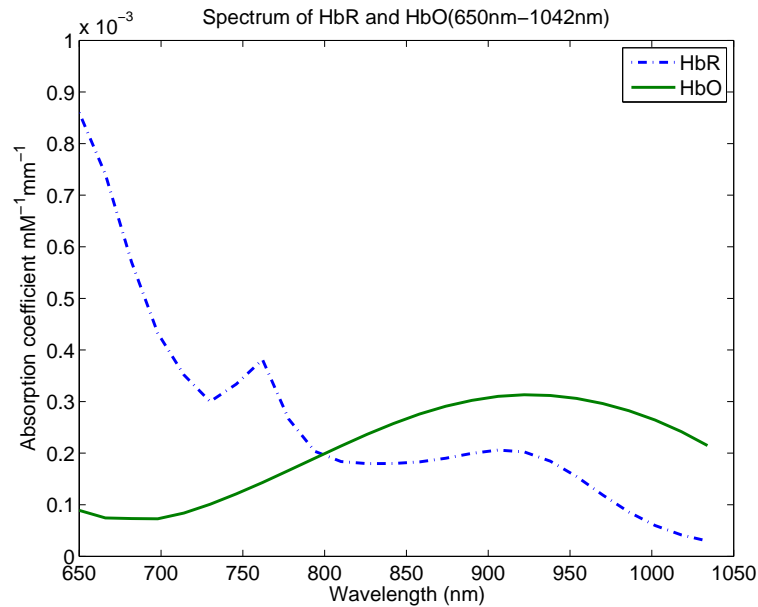


Figure 3.11 Absorption spectrum for HbO and HbR. Values taken from Cope et al. (1991) [48].

be considered to be constant and oxygen independent, the concentration of melanin in tissue will directly affect the reflectance of light from the skin and therefore the transmission of light into the tissue below [47].

Hemoglobin

Figure 3.11 shows the specific absorption coefficients of HbO and HbR in the wavelength range 450 - 1000 nm. The difference in the absorption spectra explains the well recognized phenomena of arterial blood (containing approximately 98% *HbO*) having a bright red appearance while venous or deoxygenated blood appears more blue. In the NIR region of the spectrum the absorption of both chromophores decreases significantly compared to that observed in the visible region. However the absorption spectra of *HbR* and *HbO* remain significantly different in this region allowing spectroscopic separation of the compounds to be possible using only a few sample wavelengths. An isobestic point where the specific absorption coefficients of the two compounds are equal can be seen at around 800 nm, which can be used to calculate hemoglobin concentration independent of oxygen saturation [47].

3.2.1.2 Scattering. Scatter of light in tissue is due to the spontaneous variations in the refractive index at microscopic and macroscopic scales. It is due to several optical effects; a) reflection and refraction of light from interfaces between materials having different refractive indices, b) reflection of light by discrete particles in the tissue ranging from organic molecules to whole cells, c) absorption of light rays by atoms and molecules and re-radiation at the same wavelength but in other directions [49]. For example, scattering occurs at membrane boundaries of the cells themselves as well as at boundaries between various organelles inside the cell. As in absorption, the volume of a particular scatterer within the tissue is as important as its scattering ability [47]. Scattering in turbid media is described by the scattering coefficient, which is defined as the probability of scattering per unit length; and describes the average of how many times per unit length a photon change its direction. In tissue, scattering is not isotropic, but forward directed [50].

The propagation of light through a homogeneous medium that is highly scattering. Biological tissue is a highly scattering medium and light travelling through tissue is therefore subjected to numerous scattering events and is also absorbed by various compounds within tissue (Figure 3.12). In the adult head, light must first penetrate skin, skull and cerebrospinal fluid before reaching the grey and white matter of the cerebral cortex. Previous studies have been reported the optical properties of the each layer of the brain (Table 3.2) [51, 52]. The skin and scalp are highly scattering, as is the cerebral cortex. The CSF layer, which lies in between, has very low scattering properties and this has a significant effect on light propagation. It confines the penetration of light to the shallow region of the grey matter, with few photons probing the white matter.

3.2.1.3 Modified Lambert Beer Law, Hb, HbO Calculations. In order to determine the contribution of multiple chromophores (e.g., HbR and HbO), we must take measurements at one or more wavelengths per chromophore to be resolved. For example, by measuring the change in light intensity at two wavelengths, and using the known absorption coefficients of *HbO* and *HbR* at those wavelengths (Figure 3.11), one

Table 3.2
Thickness and Optical properties (NIR range) of Tissue in Adult Head [52, 51].

Tissue Type	Thickness (cm)	Scattering Coefficient μ_s (mm ⁻¹)	Absorption Coefficient μ_a (mm ⁻¹)
Scalp	0.3-1	1.9	0.018
Skull	0.5-1	1.6	0.016
CSF	0.2	0.25	0.004
Grey matter	0.4	2.2	0.036
White matter	-	9.1	0.014

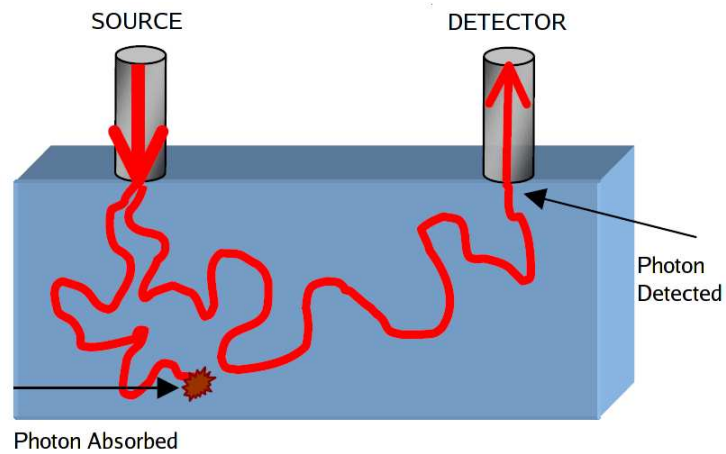


Figure 3.12 The propagation of light through a homogeneous medium that is highly scattering. There are some photons being detected due to the scattering while others are absorbed.

can then separately determine the concentration changes of HbO and HbR by solving the two equations with two unknowns for Hb and HbO (Eq.3.21, 3.24, 3.25, 3.26). This approach can be generalized to more than two wavelengths.

$$I_L = I_0 e^{-\varepsilon(\lambda)CL} \quad (3.23)$$

$$OD(\lambda) = \log(I_0/I_L) = \varepsilon(\lambda)CL \quad (3.24)$$

$$\Delta OD(\lambda_1) = (\varepsilon_{HbO_2}(\lambda_1)\Delta[HbO_2] + \varepsilon_{Hb}(\lambda_1)\Delta[Hb])LB(\lambda_1) \quad (3.25)$$

$$\Delta OD(\lambda_2) = (\varepsilon_{HbO_2}(\lambda_2)\Delta[HbO_2] + \varepsilon_{Hb}(\lambda_2)\Delta[Hb])LB(\lambda_2) \quad (3.26)$$

These equations represent the changes in the total light attenuation signal with respect to absorption coefficients of the corresponding tissues. L is the mean free pathlength and $B(\lambda)$ is the correction of this pathlength with respect to wavelength. Given equations 3.25 and 3.26, and assuming $B(\lambda_1) \cong B(\lambda_2) = B$, $\Delta[HbO_2]$ and $\Delta[Hb]$, the changes in $[HbO_2]$ and $[Hb]$ concentrations; respectively, can be calculated from equations 3.25 and 3.26 as:

$$\Delta[Hb] = \frac{OD(\lambda_1) - \frac{\varepsilon_{HbO_2}(\lambda_1)}{\varepsilon_{HbO_2}(\lambda_2)}OD(\lambda_2)}{LB[\varepsilon_{Hb}(\lambda_1) - \varepsilon_{Hb}(\lambda_2)\frac{\varepsilon_{HbO_2}(\lambda_1)}{\varepsilon_{HbO_2}(\lambda_2)}]} \quad (3.27)$$

$$\Delta[HbO_2] = \frac{OD(\lambda_1) - \frac{\varepsilon_{Hb}(\lambda_1)}{\varepsilon_{Hb}(\lambda_2)}OD(\lambda_2)}{LB[\varepsilon_{HbO_2}(\lambda_1) - \varepsilon_{HbO_2}(\lambda_2)\frac{\varepsilon_{Hb}(\lambda_1)}{\varepsilon_{Hb}(\lambda_2)}]} \quad (3.28)$$

from which total blood volume change (tHb) and oxygenation can be estimated by:

$$\Delta[BV] = \Delta[HbO_2] + \Delta[Hb] \quad (3.29)$$

$$\Delta[Oxy] = \Delta[HbO_2] - \Delta[Hb] \quad (3.30)$$

3.3 Other Neuroimaging Modalities

In addition to fMRI and fNIRS, there are other neuroimaging methods that are readily available to clinical neuroscientists for neuroimaging. Some of these methods measure neuronal activity directly, namely EEG and MEG, while the other modalities use indirect measures resulting from neural activity i.e. blood flow and metabolic effects, namely PET.

3.3.1 EEG/MEG

Electroencephalography (EEG) measures the electrical activity of the brain by recording from electrodes that are placed on the scalp. The measurements of the EEG are of voltage differences between different parts of the brain; these voltage differences are representative of the electric signal elicited from postsynaptic potentials of large numbers of neurons.

The electrical activity of the neurons in the brain generates electromagnetic fields, which can be measured externally. Magnetoencephalography (MEG) is the recording of these electromagnetic fields. MEG uses superconducting quantum interference devices (SQUIDs) that can detect magnetic fields as small as femtoteslas ($1\text{fT} = 10^{-15}\text{ T}$). The MEG (and EEG) signals derive from the net effect of ionic currents flowing in the dendrites of neurons during synaptic transmission. In order to generate a signal that is detectable, approximately 50,000 active neurons are needed [53].

The advantage of EEG and MEG is temporal resolution in terms of millisecond. The source localization of neuronal activity with EEG and MEG is compromised by the inverse localization problem. Multiple ways have been developed to overcome the inverse localization problem by combining multimodality data [54, 55]. After solving the inverse problem, the sources can be overlaid on a registered high resolution MR image on the brain surface on areas known to be active during that functional task. This enables spatiotemporally accurate detection of brain function.

3.3.2 PET

Positron Emission Tomography (PET) depends on detecting positrons emitted radio labeled tracers injected into the blood stream. Using different isotopes, the brain tissue metabolism and blood flow can be detected [56]. PET has the advantage that the biological variables can be calibrated in terms of absolute physical quantities such as metabolic rates in mg of a substance consumed per minute per unit volume of tissue. Particular radio-labeled tracers are used for particular measurements; PET isotopes can be labeled to most organic molecules. For example, ^{18}F -labeled deoxy-2-fluoro-D-glucose (^{18}F -FDG) can be used to quantify regional cerebral glucose utilization, which usually correlates with regional synaptic activity [10, 57]. ^{15}O labeling can help to measure regional cerebral blood volume (rCBV) or regional cerebral blood flow (rCBF) using ^{15}O -CO and ^{15}O -H₂O, respectively [58]. The main disadvantages come from the reliance on radioactivity.

3.4 Multimodality Neuroimaging Approaches

All techniques mentioned above are trying to measure hemodynamic/metabolic and electrical changes during neuronal activities. However, each method is limited to its sensitivity profile. This causes to see the whole picture with some missing parts (Figure 3.13). Recently the multimodality approaches in neuroimaging have given a much more precise spatiotemporal picture of the functional activities in the brain. By fusing multiple imaging and detection techniques, we can use the complementary strengths and overcome the limitations of the individual neuroimaging methods [59]. The multimodality methods allow one to hypothesize the correlations between measured variables and give ideas why and how the measured changes take place [59].

In contrast to fMRI, EEG measures neuronal currents directly from the subject's scalp with a high temporal resolution in the range of milliseconds. However, determining the exact location of the current sources is difficult due to the so-called "inverse problem" of the EEG and the lack of precise information regarding individual geometry

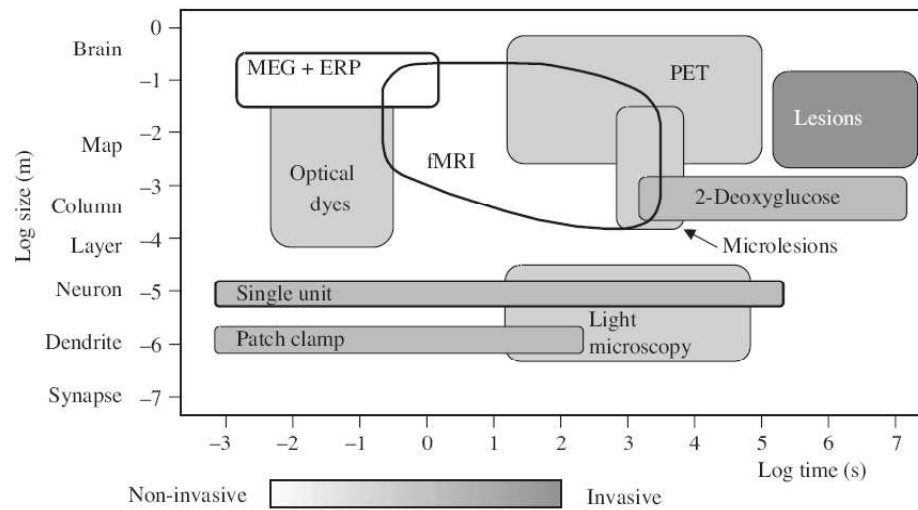


Figure 3.13 An illustration of the relative spatial and temporal sensitivities of different functional brain mapping methods that can be used in animals, man, or isolated tissue preparations [60].

and conductivity as well as the limited number of EEG channels. By combining EEG and fMRI one hopes to overcome the spatial limitations of EEG and the temporal limitations of fMRI by utilizing their complementary features [61, 62, 63, 64, 65, 66, 67, 68].

The work combines the functional imaging of ASL MRI, which captures the blood flow in the brain, and PET scanning, which looks at the glucose metabolism in the brain [69]. This novel approach for concurrent measurement of regional CBF and regional cerebral metabolic rate for glucose consumption (CMRGlc) in humans is proposed and validated in normal subjects during visual stimulation [69]. ^{18}F -labeled fluorodeoxyglucose was administered during the measurement of CBF by continuous ASL MRI. An excellent concordance between regional CBF and regional CMRGlc during visual stimulation was found, consistent with previously published PET findings.

Simultaneous MRI acquisition of CBV, CBF, and BOLD information during brain activation can also be considered within the concept of multimodality imaging techniques. Specifically, MRI Pulse sequences such as DW EPI, ASL and GE EPI have been designed to measure CBV, ASL, and BOLD. It was reported that this kind of multimodality approach was able to be utilized in fMRI experiments, with potential advantages of obtaining accurate transient information of the activation-

induced hemodynamic responses [70, 71, 72, 73, 74, 75].

Optical imaging methods, including NIRS, have been combined with BOLD fMRI in order to reveal new correlations between hemodynamic and metabolic changes with respect to BOLD signal changes during brain activation [76]. fNIRS has the potential to elucidate some key issues concerning the basis of the vascular response, since it measures the physiological quantities total and deoxygenated hemoglobin concentration - which are the major constituents of BOLD signal changes. In addition to this, while optical measurements are poorer in spatial resolution and depth penetration than fMRI, they provide information about changes in physiological quantities with a high temporal resolution [77, 78, 76, 79]. Furthermore, while fNIRS can measure changes in blood volume (tHb), MRI can measure changes in blood flow via ASL. Thus, through the combination of fNIRS and MRI one should be able to obtain an accurate estimate of dynamic changes in $CMRO_2$ during brain activation [80].

In this dissertation research, we used fNIRS-fMRI multimodality approach to investigate the BOLD signal. Using fNIRS, we recorded concentration changes both HbO and HbR as well as tHb. This provides a useful link between BOLD signal between blood oxygenation and CBV.

4. Physiological Background of BOLD Signal and Balloon Model

In the temporal relationship between functional changes in CBF and CBV, an elemental aspect of cerebrovascular physiology, is poorly understood. Hence there is need for developing hemodynamic models which quantitatively/qualitatively associate blood flow (CBF) and CMRO_2 with HbR, oxyhemoglobin (HbO), and total hemoglobin (tHb) measured by different imaging modalities such fNIRS and BOLD-fMRI signal. To do that, Buxton et al. (1998) developed a mechanistically compelling model of how evoked changes in blood flow were transformed into a blood oxygenation level dependent (BOLD) signal [1]. A component of the Balloon model, namely the relationship between blood flow and volume, was then elaborated in the context of standard windkessel theory [81]. An extensive discussion regarding the biophysical modelling which this is based on is discussed in this chapter

4.1 BOLD Physiology

Like the PET, the BOLD-fMRI is an indirect measure of neural activity. fMRI has been used to measure neuronal metabolic activity [82, 83, 84]. BOLD fMRI signal reflects combined effects of several physiological parameters like CBF, CBV and CMRO_2 during the neuronal activity. Although it is an indirect measurement, it has been shown that positive BOLD changes correlated with Local Field Potential (LFP) which suggests that the BOLD signal reflects the synaptic activity, which is directly related to stimulus processing [16]. Within the concept of this correlation, following a neuronal activity, CBF increases dramatically, CBV increase moderately, and CMRO_2 increases by a much smaller amount. Therefore, all these physiological activities result in a decrease in the amount of HbR within the tissue so the MR signal increases (Figure 4.1(a), 4.1(b)).

On the other hand, combined effects of all three physiological parameters could

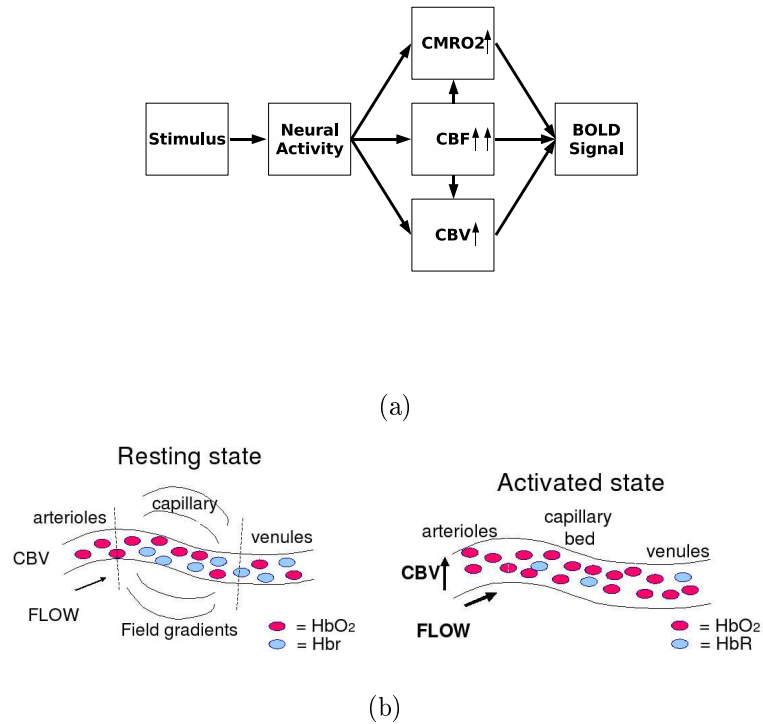


Figure 4.1 The events that generates BOLD signal [14].

be observed as three transients in BOLD response as the initial dip, the positive BOLD and the post stimulus undershoot (PSU) [2] (Figure 4.2).

4.1.1 Initial Dip

The initial dip is potentially one of the most important but controversial aspects of the BOLD response. It is accepted as the fast response of the neuronal activity. It was first observed in optical intrinsic signal (OIS) study [85]. In this study [85], a rapid increase HbR and decrease in HbO was found. It was explained as a rapid increase of oxygen extraction (E). Later studies, however, found only HbR increase but no change in HbO. This increase in HbR is reflected in an initial dip in the fMRI. It has been interpreted as an increase in CBV and E. First hypothesis assumes an increase of CBV following the neuronal activity [1] (Figure 4.3(a)). However, later a new hypothesis proposed. This hypothesis assumes a slight delay of the CBF response compared to the CMRO₂ response [86] (Figure 4.3(b)).

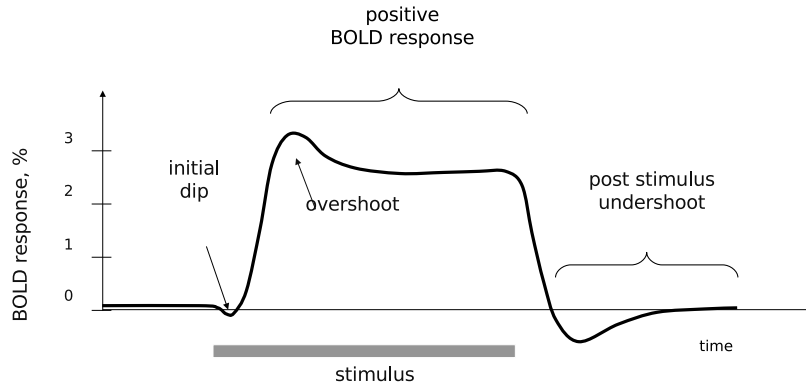
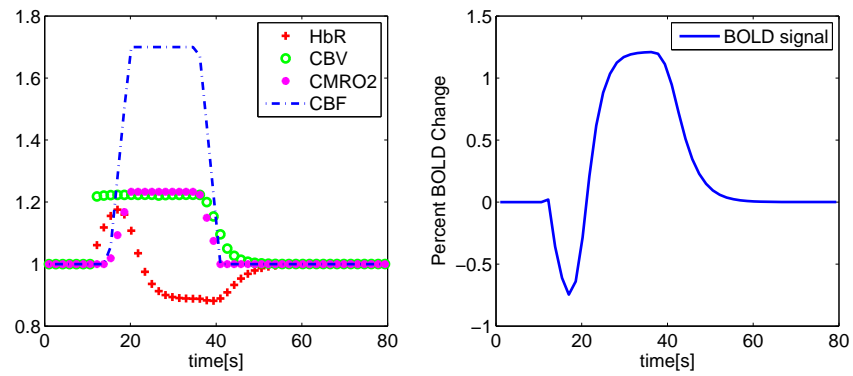
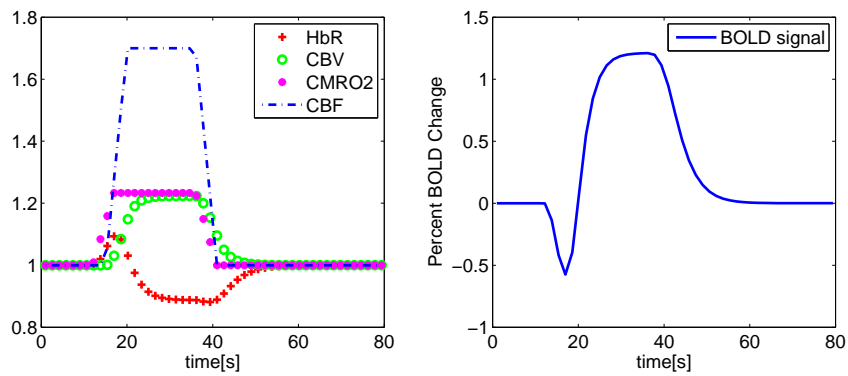


Figure 4.2 An illustration of BOLD response which indicates three transients, initial dip, positive BOLD and post stimulus undershoot.



(a)



(b)

Figure 4.3 (a) CBV based initial dip (b) CMRO₂ based initial dip.

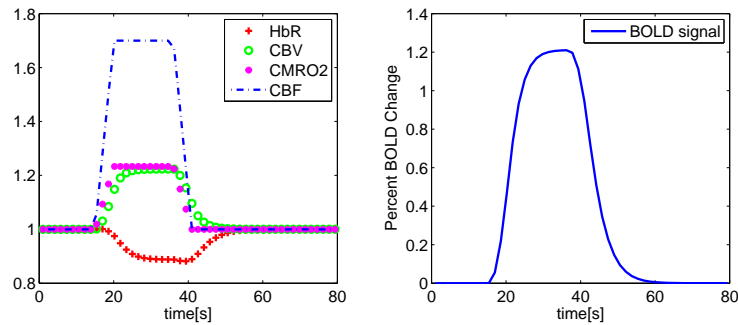


Figure 4.4 An illustration of positive BOLD transient. CBF increase exceed the demands of CMRO_2 . This causes sudden decrease in HbR concentration.

4.1.2 Positive BOLD

This is best identified part of the BOLD signal. Following the increased neural activity in the brain, the local CBF increases much more than the CMRO_2 [87]. This results in a drop in the oxygen extraction and HbR which generates a positive BOLD signal change (Figure 4.4).

4.1.3 Post Stimulus Undershoot

The cause and significance of the post stimulus undershoot have been a source of speculation the beginning of the fMRI [84]. The source of this deflection is an alteration of the local concentration of HbR which means that the change of T_2^* weighted signal towards negative polarity is thought to be an increase in HbR. This definition is consistent with the optical imaging studies which observed an increase in HbR and a decrease in HbO concentration [88, 89]. At the end of the stimulus the signal dipped below the baseline level and remained depressed for a considerable time (tens of seconds). This pattern is often seen when the stimulus (active) and the control (rest) periods are the same [90].

From the basic physical theory of BOLD effect, signal change observed in fMRI is due to the the alteration in HbR concentration. The post stimulus undershoot is a transient effect which is due to the fact that some physiological quantities return to baseline slowly at the end of the stimulus. Changes in CBF, CMRO_2 and CBV

are potential sources of the undershoot. Following hypothesis has been proposed for possible physiological changes which generate post stimulus undershoot at the end of BOLD signal.

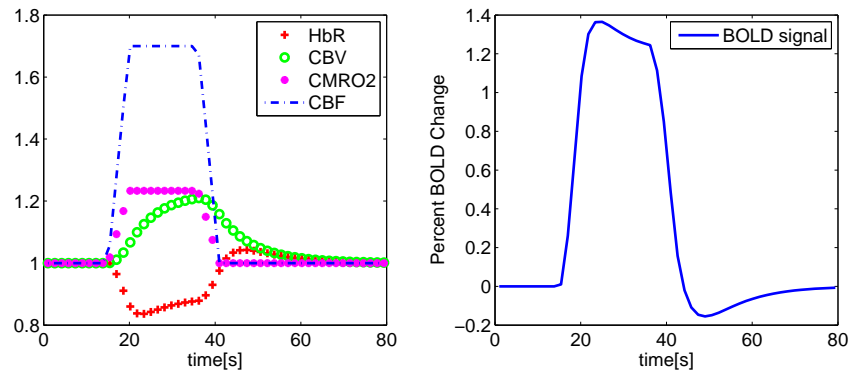
Experiments have reported an evidence that elevated blood volume associated with activation is slow to return after the end of the stimulus [81]. They used a long lasting intravascular contrast agent to monitor the blood volume dynamics during activation and laser Doppler Flowmetry to measure CBF with the same experimental protocol. The temporal curves showed quick return of CBF to baseline but an elevated CBV with a time lag that coincides with BOLD post stimulus undershoot (Figure 4.5(a)). In addition to this study, several studies have measured post stimulus undershoot due to the slow return of CBV [35, 1].

The next hypothesis for the post stimulus undershoot would be that CBF itself dips below the baseline. If the flow dropped below the baseline while $CMRO_2$ stays approximately stays at baseline, more oxygen would be extracted, the HbR content would be increase and as a result of this BOLD signal would be decrease, producing the post stimulus undershoot (Figure 4.5(b)). Several studies have reported a CBF undershoot which support this hypothesis [91, 92, 93].

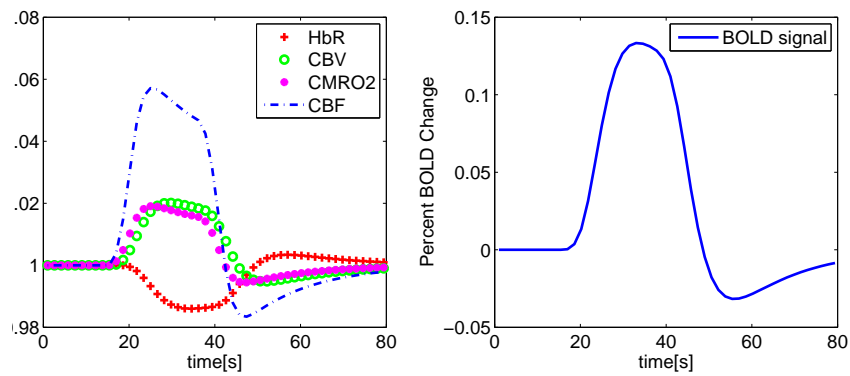
The last hypothesis proposes that CBF returns to baseline while $CMRO_2$ remains elevated within the duration of the post stimulus undershoot. This hypothesis was reported by several studies [94, 95, 96, 97]. At the end of the stimulus, CBF returns to baseline more quickly that $CMRO_2$, and so HbR concentration is increased above the baseline, producing the post stimulus undershoot (Figure 4.5(c)).

4.2 Balloon Model

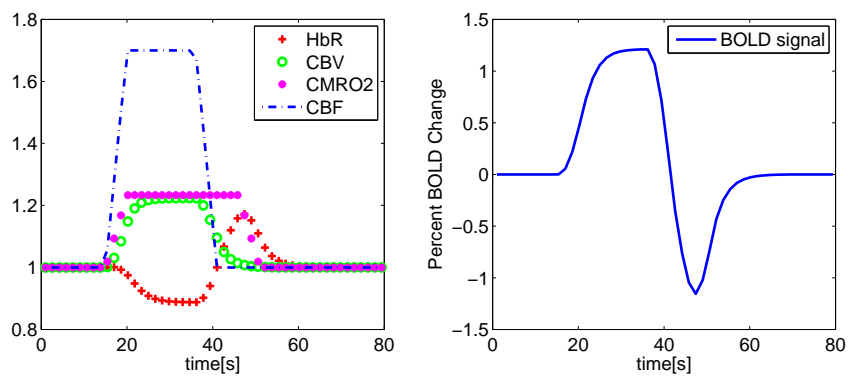
Balloon model is based on a few basic assumptions. Although these assumptions are simple, it simplifies BOLD signal to understand in terms of several physiological parameters such as CBV, HbR concentration and CBF. Basic physical picture repre-



(a)



(b)



(c)

Figure 4.5 An illustration of post stimulus undershoot due to (a) delayed return of CBV (b) CBF undershoot below the baseline (c) continuation of CMRO_2 with respect CBF termination.

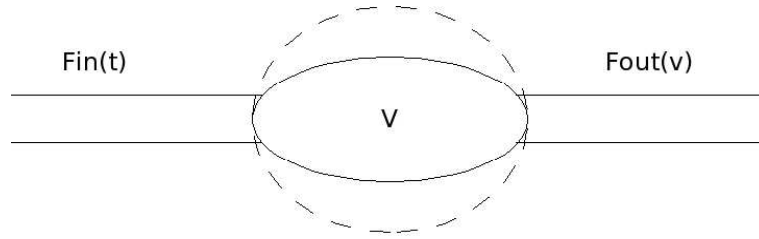


Figure 4.6 The balloon model [1]. It is assumed in the model that the vascular bed (CBV) within a small volume of tissue can be modeled as an expandable venous compartment (a balloon) that is fed by the output of the capillary bed. V is the volume of the balloon, F_{in} is the inflow, and F_{out} is the outflow from the balloon.

sented by the balloon model is as follows: The capillary bed is treated as a fixed set of pipes assumed to be undispensible (Figure 4.6). The small, post capillary veins, however, are distensible and changes in blood volume all occur on the venous side. Arterioler dilation is assumed to be a negligible change in terms of CBV. The vascular bed within a small volume of tissue is then modeled as an expandable venous compartment (balloon) that is fed by the output of the capillary bed. The volume flow rate into tissue is an assumed function of time that drives the system. The volume flow rate out of the system is assumed to depend primarily on the pressure in the venous compartment. This pressure depends on volume of the balloon. The amount of swelling of the venous balloon is modulated by the biomechanical properties of the vessel (pressure/volume curve), in terms of the difference between the driving force, the flow in ($F_{in}(t)$ or CBF), and the flow out (F_{out}), which is a function of the venous volume V_v . For simplicity, Balloon model neglect the capillary contribution and assume that all of the HbR ($q(t)$) is in the venous compartment. The rate of entry of HbR into the venous compartment is $F_{in}EC_a$, where E is the net extraction of O_2 , from the blood as it passes through the capillary bed and C_a , is the arterial O_2 , concentration (assumed to be due to a fully oxygenated hemoglobin concentration, 100%). The clearance rate of HbR from the tissue is $FQ(t)/V(t)$ ($Q(t)/V(t)$, the average venous concentration) [1]. The equations of the balloon model represent mass conservation for blood and HbR as they pass through the venous balloon:

$$\frac{dq}{dt} = \frac{1}{\tau_0} \left[f_{in}(t) \frac{E(t)}{E_0} - \frac{q(t)}{v(t)} f_{out}(v, t) \right] \quad (4.1)$$

$$\frac{dv}{dt} = \frac{1}{\tau_0} [f_{in}(t) - f_{out}(v, t)] \quad (4.2)$$

All the variables in the equations are scaled to their initial conditions ($t=0$), $q(t) = Q(t)/Q_0$, $v(t) = V(t)/V_0$, $f_i(t) = F_{in}(t)/F_0$, and $f_o(v) = F_{out}(v)/F_0$. Therefore, each variables is dimensionless and before the activation (rest condition) $q = v = f_{in} = f_{out} = 1$. τ_0 is the mean transit time through the balloon at rest. However, there are two functions that remain to be specified: $E(t)$ and $f_{out}(v)$. The oxygen extraction fraction E was modeled by the oxygen limitation model as:

$$E(t) = 1 - (1 - E_0)^{\frac{1}{f_{in}}} \quad (4.3)$$

CMRO₂ ($m(t)$) then is modelled as follows:

$$m(t) = \frac{E(t)}{E_0} f_{in} \quad (4.4)$$

Experimental studies of altered flow states have reported that relationship between CBV and CBF can be written by an empirical power law as follows (Figure 4.7(a)) [98]:

$$CBF = CBV^\alpha \quad (4.5)$$

However, experimental measurements, using a vascular contrast agent, sug-

gested that although the steady-state relationship was in reasonable agreement, but the transition periods were not [81]. Following equation for this nonlinear relationship proposed [1]:

$$f_{out}(v, t) = v^{\frac{1}{\alpha}} + \tau \frac{dv}{dt} \quad (4.6)$$

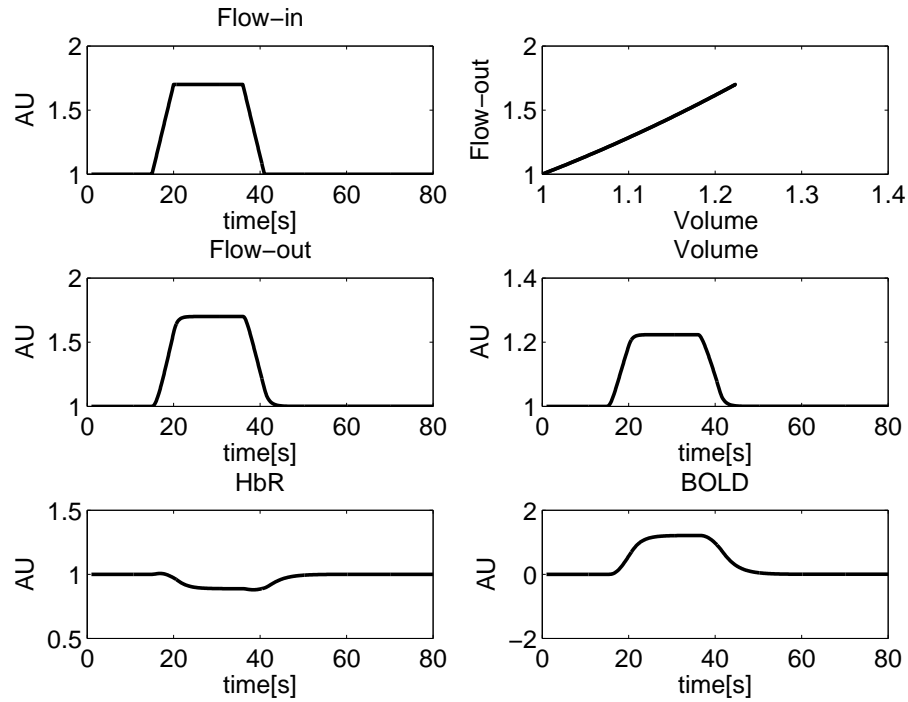
The time constant τ controls how long this transient adjustment requires. A nonzero value for τ produces hysteresis in the curve $f_{out}(v)$ (Figure 4.7(b)), so that the system follows a different curve on inflation and deflation. To generalize this form and enable more fine tuning to data, we allow τ to take on different values during inflation (τ_+) and deflation (τ_-).

$$\tau = \left\{ \begin{array}{l} \tau_+ \quad \frac{dv(t)}{dt} \geq 0 \\ \tau_- \quad \frac{dv(t)}{dt} < 0 \end{array} \right\}.$$

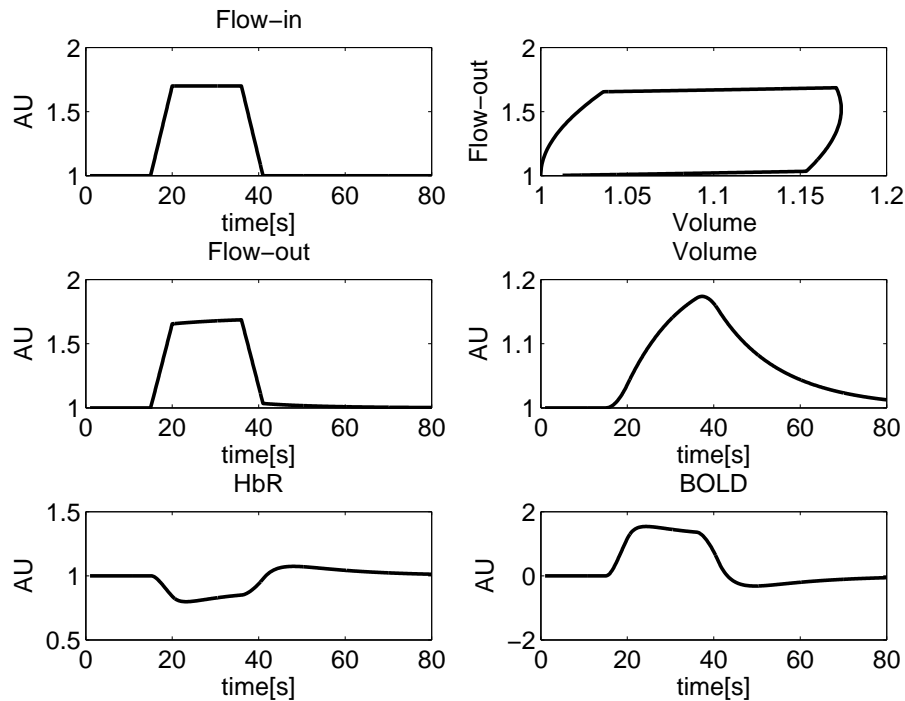
Combining these expressions, fractional BOLD signal can be written as follows [1]:

$$\frac{\Delta S}{S} = V_0 \left(k_1(1 - q) + k_2 \left(1 - \frac{q}{v} \right) + k_3(1 - v) \right) \quad (4.7)$$

The parameters k_1 , k_2 , and k_3 , are dimensionless and can be estimated from the earlier work [43]. For $B_0 = 1.5$ T and TE = 40 ms, k_1 is $7E_0$, based on the numerical studies of [43], where E_0 , is the resting oxygen extraction fraction. Based on the results of previous study [33], k_2 is equal to 2 and k_3 is $2E_0 - 0.2$. V_0 is the actual venous blood volume fraction (e.g., 1-4%). A detailed derivation of Eq. 4.7 is given in the



(a)



(b)

Figure 4.7 Different balloon model simulation based on (a) linear volume changes of the power law, $CBF = CBV^\alpha$, (b) on modified nonlinear volume changes for the viscoelastic effects, $f_{out}(v, t) = v^{\frac{1}{\alpha}} + \tau \frac{dv}{dt}$. The volume change in this example is to illustrate the type of transients that can arise. BOLD signal shows a initial overshoot, followed by slight return to a plateau and ending with a strong post stimulus undershoot. Model parameters in this simulations are: for (a) $\alpha = 0.38$, $E_0 = 0.4$, $V_0 = 0.02$, $\tau_0 = 3$, for (b) $\alpha = 0.38$, $E_0 = 0.4$, $V_0 = 0.02$, $\tau_0 = 3$, $\tau = 20$.

appendix of [1].

4.2.1 Balloon Model Improvements

An extension of the Balloon model in terms of linking CBF to physiological parameter has published by Friston et al. (2000) [99]. In this study, balloon model extended to incorporate the dynamics of CBF induction by synaptic activity, is sufficient in reproducing the main non-linearities observed in evoked fMRI responses. Later, Buxton et al. (2004) [2] proposed following equation in order to link CBF to neuronal activity.

$$f_{in}(t) = 1 + (f_1 - 1)h(t - \delta f) * N(t) \quad (4.8)$$

The symbol $*$ denotes convolution. The parameter f_1 scales the response shape to the appropriate amplitude and represents the normalized flow increase on the plateau of the CBF response to a sustained neural activity with unit amplitude. For example, if $N(t)$ is a duration of the stimulation block with amplitude 1. The parameter δf is the delay after the start of the stimulus before the CBF response begins. $h(t)$ is a gamma-variate function with a full width at half maximum (FWHM) of about 4 s. However, all these models does not have any sensitivity to blood gases. In this dissertation, blood gases have been added in terms of partial pressure of CO₂ (PaCO₂).

The effects on cerebral circulation of CO₂, an end product of cellular metabolism have been studied extensively and are well known [100, 98, 24, 23, 101, 102, 103]. An increase in the blood CO₂ level leads to decrease in pH via the bicarbonate reaction. The tone of cerebral vascular smooth muscle is sensitive to this pH level in the vicinity of the blood vessel. For instance, vasodilation occurs along with a decrease in extracellular pH. Therefore an increase in PaCO₂ causes a global increase in CBF. The CMRO₂ of oxygen consumption is not increase by an increase in CO₂ tension [103]. Therefore,

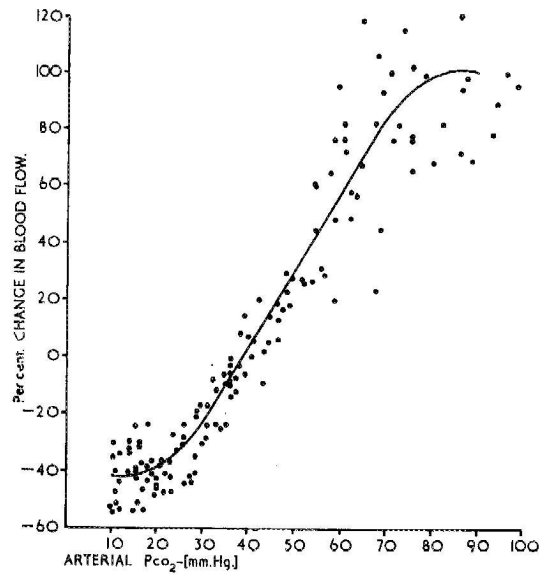


Figure 4.8 The effect of alteration in PaCO_2 in animals on the CBF. Zero reference line for CBF is PaCO_2 of 40 mmHg [110].

when CBF increases and CMRO_2 remains constant in the tissue, the oxygen saturation of the venous circulation increases and the concentration of HbR decreases. Therefore, BOLD signal transients should qualitatively mimic the CBF and change monotonically with the change in PaCO_2 [104, 105, 106, 107].

The relation between CBF and PaCO_2 was described as an exponential function, with a moderate CBF changes during hypocapnia, and pronounced changes during hypercapnia [103]. It is known from following studies, both in humans and animals, the slope of the curve decreases at extreme PaCO_2 , so that its true shape replaced to sigmoid rather than exponential. In normal individuals, the overall relationship between PaCO_2 and CBF is sigmoid, but it is linear between 25-65 mmHg [108, 109]. These results were in agreement with the previous animal studies (Figure 4.8) [110].

There are extensive biophysical models which investigate the CBF- PaCO_2 relationship [111, 112, 113, 114, 115]. However, current version of Balloon model does not include any autoregulation parameters such PaCO_2 or PaO_2 [2]. A successful improvement should be appended to balloon model to reproduce, at least qualitatively, the way a healthy brain circulation responds to changes in a variety of stimuli, blood CO_2 levels, blood oxygenation, and functional activity of the brain. In this dissertation

research, balloon model is extended by adding PaCO_2 a parameter which drives the balloon model.

5. Multimodal Investigation of fMRI and fNIRS derived Breath Hold BOLD Signals with an Expanded Balloon Model

5.1 Introduction

Local paramagnetic HbR concentration is the source of BOLD signal. HbR concentration changes cause MRI signal changes by altering the local susceptibility of blood around the vessels. However, fMRI as an indirect measurement does not provide a detailed understanding of the underlying physiology, since the BOLD signal is sensitive to all spatial scales of vessels and combined effects of several physiological parameters like CBF, CBV and CMRO₂. fNIRS provides detailed biochemical specificity in the form of HbR and HbO concentration changes. While fNIRS offers a unique opportunity to track the concentration changes of these two molecules within a microvascular space with high temporal resolution [116, 117], it suffers from limited penetration depth and low spatial resolution [118, 119, 120]. Thus, a multimodal measurement approach using fNIRS and fMRI may synergize and overcome these limitations. Several recent studies compared the hemodynamic response brain activation as measured by fNIRS with fMRI [77, 121, 122, 79, 78, 123, 124, 76, 125, 126, 127]. Toronov et al. (2003) [128], Boas et al. (2003) [80] and Hoge et al. (2005) [122] have employed biophysical models to relate their fNIRS measurements to fMRI measurements. In addition to brain activity studies, multimodality approaches using fNIRS and fMRI have been performed to measure Vasomotor Reactivity (VMR) and transient global changes in hemodynamics brought on by hypercapnia during the breath holding task [129, 130]. While all these studies have mostly focused on the correlation of the BOLD signal to the changes in the hemoglobin concentrations, detailed multimodal studies are needed to be done to explore the transient features of hemodynamic response such as the overshoot and undershoot [3]. In order to fully unveil the underlying physiology of these transients of hemodynamic response, a comprehensive balloon model describing BOLD signal as a function of CBV, CBF and HbR should be utilized as a guide in these multimodal studies.

In the last decade, fNIRS has explored several clinical applications. It has been devoted to the assessment of VMR in subjects affected by acute and chronic pathologies: microangiopathy [131], migraine [132, 133, 134, 135], carotid artery occlusion [136], sleep apnea [137, 138, 139]. In addition, by manipulating blood gas tensions it is possible to assess VMR by NIRS. In practice, VMR is usually manipulated by means of direct CO₂ inhalation (usually between 5 % and 7 % concentration), or by means of simple BHT. These make fNIRS possible to quantify VMR by looking at the concentration changes of HbR and HbO. These methods have been extensively used in fMRI to investigate characteristic differences of BOLD response patterns [140, 75, 104, 141, 142, 143, 144, 145, 146, 106, 107].

The aim of the present study is to interpret transients of fNIRS and fMRI measurements during BHT with an expanded balloon model (EBM). It has been shown that simple BHT offers a convenient method of assessing CO₂ reactivity without requiring CO₂ administration [147]. To include the BHT effects, we integrated simulated PaCO₂ changes as a driving function to the balloon model rather than CBF (Figure 5.1).

5.2 Methods

5.2.1 Subjects and Study Design

4 healthy subjects (3 male ages 25 ± 1 and 1 female age 26) were recruited for this study. Written consents were obtained from all subjects after complete description of the study prior to the first session. fMRI and fNIRS measurements were conducted asynchronously, but a computer that houses a digital-analog card recording all timing signals including imaging specific synchronization signals (gradient waveforms for MRI, optical sync signals for fNIRS) allowed careful temporal registration of both measurements for comparative analysis. In both cases, subjects were positioned in supine and asked to breath normally during rest periods. After an initial 90 seconds of rest, they were asked to exhale all the air and hold their breaths for 30 seconds. In order to

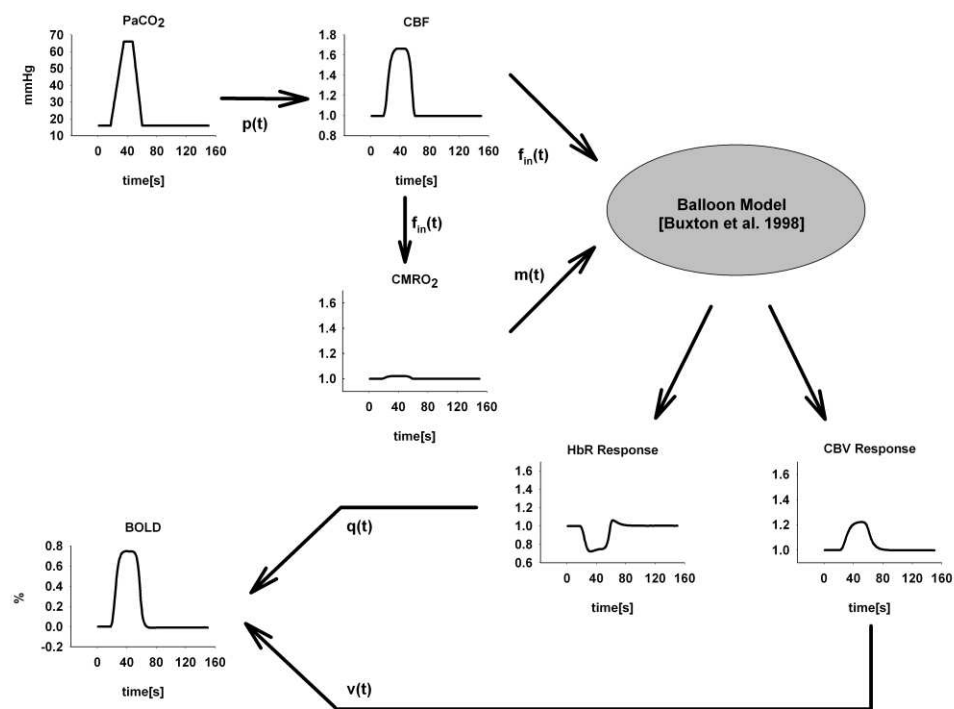


Figure 5.1 Diagram of the proposed model linking the applied BHT to the resulting physiological responses and the measured BOLD response. PaCO₂ was used as a driving function of balloon model instead of CMRO₂ and CBF.

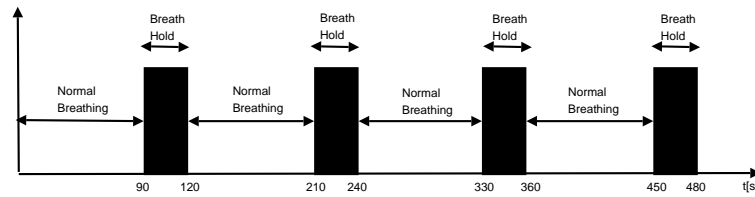


Figure 5.2 Experimental protocol with 4 repetitions of 90 second normal breathing followed by 30 second BHT.

obtain post stimulus undershoot effect, a relatively longer rest block, 90s, was chosen [90]. This cycle is repeated four times for each subject. The protocol timing diagram can be seen in Figure 5.2.

5.2.2 fNIRS

The fNIRS system was developed at the Bogazici University Biophotonics Laboratory (NIROSCOPE 201) and houses a probe that contains LED light sources and multiple photodetectors. It has been used in several clinical studies [132, 133]. The source and detectors are equidistantly placed on the probe with a source detector separation of 2.5 cm. A source-detector distance of 2.5 cm provides a penetration depth of 1.25 cm in tissue. Previous works demonstrated that with a source detector distance equal to approximately 2.5 cm the fNIRS equipment is capable of detecting effectively the HbR and HbO concentration changes on the surface of the cerebral cortex [148, 149, 150, 116, 151]. The probe is positioned such that its base aligns with the eyebrows of the subject and the middle with the Fz location from 10-20 EEG electrode placement. The concentration changes in HbO and HbR signals are calculated from the Beer-Lambert Law using two wavelengths (735 nm and 850 nm) [133, 132, 152].

5.2.3 fMRI

All experiments with fMRI were performed on Siemens Symphony 1.5 Tesla MR System at Department of Radiology, Istanbul Medical School. A single shot T_2^*

weighted gradient echo (GE) echo planar imaging (EPI) sequence was used for BOLD measurements. Seventeen transverse slices over a field of view of 192 x 192 mm with 128 x 128 resolution were acquired with a slice thickness 3 mm. Other imaging parameters were TR 2000 ms, TE 60 ms and flip angle 90 degrees. Thus, 240 BOLD-based volumes images were acquired within each experiment.

fMRI data processing was performed as follows: First, preprocessing and statistical analyses were performed using AFNI (Analysis of Functional Neuro-Images [153]). For motion correction, functional time series images were spatially registered to the first functional image (using the AFNI script 3dvolreg) and baseline drifts were removed (AFNI script 3dDetrend). The block trial data were analyzed using crosscorrelation with a boxcar reference waveform with amplitudes of 1 for the BH phases and 0 for normal breathing. Activated pixels ($P \leq 0.05$) in the first couple of millimeters of the frontal cortex identified from the correlation map were averaged to generate the BOLD signal. Then, within each subject resulting time courses were averaged for all 3 repetitions since the last breath hold transient was not completed at the end of the scan.

5.2.4 Balloon Model

BOLD responses to BHT were analyzed by the balloon model. In this model vascular bed at the venous side is modeled as an expandable balloon which is fed by arterioles [1]. Two dynamic variables; total volume of the balloon and total HbR concentration in the volume are used for expressing the balloon dynamics as detailed in the Eq. 4.1 and 4.2.

In these equations, q is the total HbR within the balloon, v (identical to CBV) is the volume of the balloon, and f_{out} is the outflow from the balloon. τ_0 is the mean transit time through the balloon at rest. We use a similar expression as Buxton et al. (1998) [1] for $CMRO_2$ ($m(t)$) with a slight modification of oxygen extraction fraction ($E(t)$) to describe the events during BHT. We chose $E_0=0.1$ which results in a max-

imum 0.02 CMRO₂ change to provide a minimally change in the oxygen metabolism. It is previously shown that CO₂ challenge during BHT does not or minimally changes the oxygen metabolism [154] and the increase of CBF leads to a diminished oxygen extraction and consequently to an increased oxygen saturation of venous blood [155].

The oxygen extraction fraction $E(t)$ and $m(t)$ is modeled as in Eq. 4.3, 4.4. Hence, we treat $m(t)$ and $E(t)$ the same as Buxton et al. (1998) [1] but use different E_0 as it is explained in the previous paragraph. We used Eq. 4.6 for relation between f_{out} and v .

Originally it was assumed that the driving function of the system, f_{in} (identical to CBF) had a trapezoidal shape [1]. In this study, we modeled f_{in} as a function of PaCO₂ and utilized a sigmoidal function describing the relationship between CBF and PaCO₂ (Figure 2.1), similar to the previous work of Lu et al. (2004) [115]. This relationship was derived from empirical data of the previous studies [22, 156, 110]. According to this relationship, the CBF changes with respect to PaCO₂ can be modeled as follows:

$$f_{in}(t) = \frac{a}{1 + e^{-b*(p(t)-c)}} \quad (5.1)$$

where, $p(t)$ is the PaCO₂ during breath hold which is assumed that it could vary between 5 mmHg to 75 mmHg as a trapezoidal function [115]. a is the scaling parameter for the CBF, b and c are the characteristic parameters of the sigmoid curve.

For each subject, EBM variables were customized to represent the signal acquired by fMRI. Then temporal comparison between the dynamic variables, q and v , were made with measured fNIRS HbO, HbR and tHb (HbO+HbR) signals. In order to represent the relationship between the model variables and fNIRS measurements, it is assumed here that the content of q within a voxel is equal to HbR. Changes in tHb

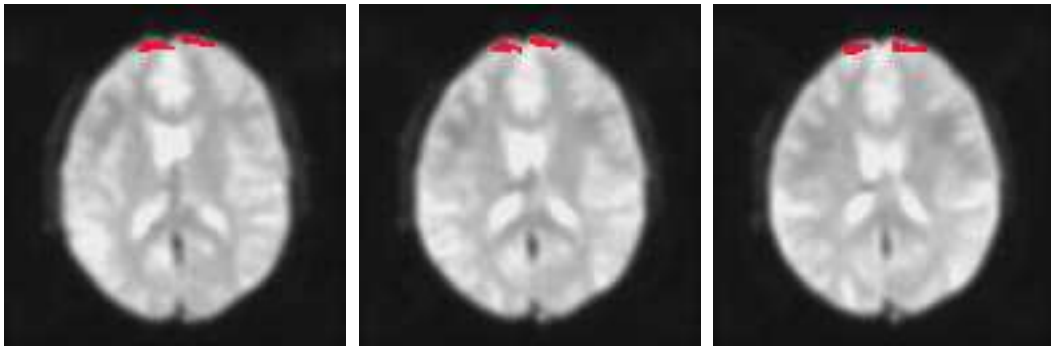


Figure 5.3 Display of selected pixels within ROI in frontal cortex on three sequential axial slices (Subject OS).

was previously demonstrated to be changes in v [136].

5.3 Results

Figure 5.3 displays the selected ROI in the pre-frontal cortex which is overlaid on functional images for one subject. Pixels in the ROI were averaged first spatially and then over all four repetitions to generate a final BOLD response time course for each subject (Figure 5.4). BOLD signal changes during the BHT varied between 0.5 - 2.2 % among different subjects.

Figure 5.5 shows averaged fNIRS HbR, HbO and tHb traces corresponding to one BHT period for all four subjects. One can see that there were two main VMR transients during BHT in fNIRS measurement. VMR transient 1 and 2 occurred within the first 10-20 and 40-50 second during BHT respectively. In VMR transient 1, three of the four subjects the fNIRS HbR concentration decreased, while the fNIRS HbO concentration increased. On the other hand, in the VMR transient 2, there were fNIRS HbO decrease and fNIRS HbR increase (see also Table 5.1).

For each subject, EBM parameters are customized to represent the signals acquired in first BOLD and then used to interpret the fNIRS measurements. Figure 5.6 illustrates BOLD signals measured by fMRI (BOLD fMRI), and signals measured by

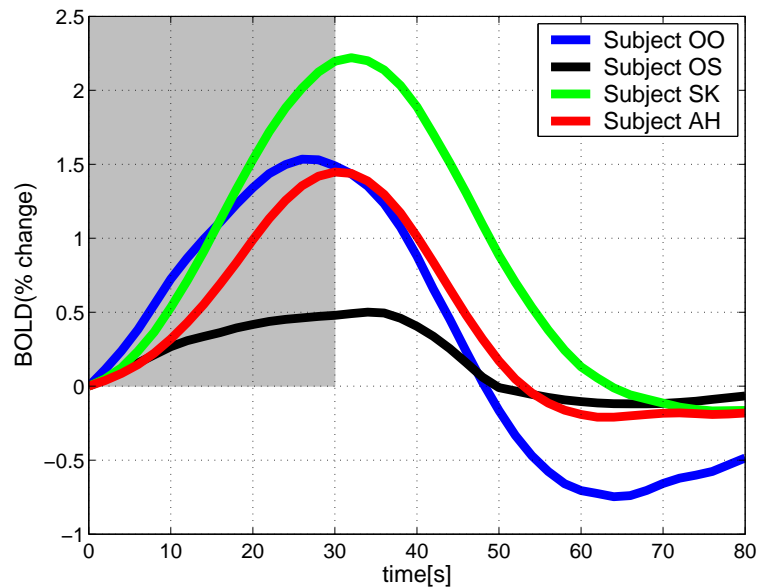


Figure 5.4 Averaged time course of BOLD signal of all four subjects. The shaded area represents the time during which the subjects performed the BHT.

Table 5.1

Numerical data obtained from simultaneous fNIRS measurements. Averaged HbO and HbR during VMR transient 1 (During 10-20th seconds of breath holding) and transient 2 (During 40-50th seconds of breath holding) traces corresponding to one BHT period. Statistical significance of paired t tests ($P < 0.05$) results indicates comparisons between HbR and HbO.

mean changes in brain oxygenation and hemodynamics						
Subjects	VMR transient 1 (10-20 s)			VMR transient 2 (40-50 s)		
	ΔHbO	ΔHbR	P Value	ΔHbO	ΔHbR	P Value
OO	0.24 ± 0.03	-0.22 ± 0.03	<0.05	-0.45 ± 0.07	0.37 ± 0.18	<0.05
OS	0.20 ± 0.03	-0.25 ± 0.06	<0.05	-0.14 ± 0.12	1.04 ± 0.20	<0.05
SK	0.01 ± 0.03	0.00 ± 0.04	<0.47	-0.34 ± 0.01	0.54 ± 0.02	<0.05
AH	0.13 ± 0.02	-0.14 ± 0.02	<0.05	-0.18 ± 0.11	0.49 ± 0.22	<0.05

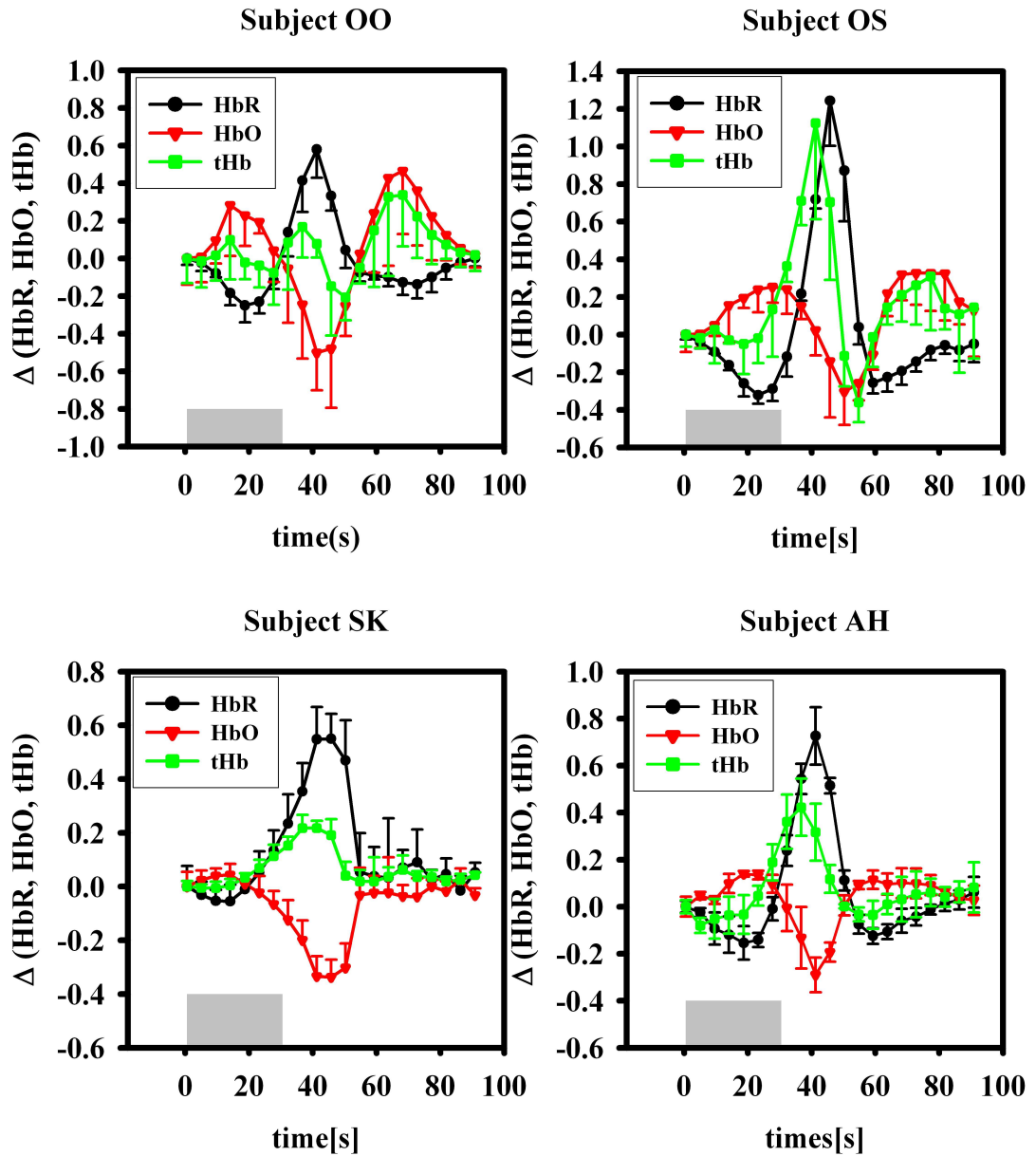


Figure 5.5 Changes in cerebral HbO, HbR and tHb obtained by fNIRS for each of four volunteers. Error bars indicate standard deviation. The shaded area represents the time during which the subjects performed the BHT.

Table 5.2

HbR peak times during post stimulus undershoot for all four subjects as measured by fNIRS and derived from individualized balloon models. Peak times are in seconds after the start of the breath hold duration.

Subjects	Peak time q (HbR) (Balloon Model)[sec]	Peak time HbR (fNIRS)[sec]
OO	41	40.5
OS	48	47.6
SK	48	48.8
AH	42	42.3

fNIRS (fNIRS HbR, HbO and tHb) for all subjects. Figure 5.6(a) indicates balloon model outputs and measurements of fNIRS while the graphs in Figure 5.6(b) shows the BOLD output of balloon model fitted to BOLD fMRI measurements. All plots in the Figure 5.6 are normalized to their maximum values and are meant to be used for detailed timing analysis [77, 157, 89]. At the beginning of the BHT, according to EBM the first parameter that increases due to the PaCO₂ raise is CBF. CBV follows it with a time delay. From the beginning of the task to post stimulus era which corresponds to VMR transient 1, HbR concentration in capillary bed is decreasing which results in the main BOLD peak. Data indicate that normalized concentration change of fNIRS HbR data decreases while fNIRS HbO increases or remains relatively constant with in this period (Figure 5.6(a)). In addition, within this period tHb which mimics the CBV starts to increase (Figure 5.6(a)). Acquired BOLD signal time courses are correlated with simulated balloon model time courses ($R^2 > 0.75$) (Figure 5.6(b)). Furthermore, during post stimulus response which corresponds to VMR transient 2 (shaded area in Figure 5.6(a)), CBF starts to decrease at the end of the breath hold and returns to baseline, while CBV decrease is slower. This also causes an increase in HbR which produces the post stimulus effect during breath hold. For the signals of fNIRS within this interval, a close coincidence of the fNIRS HbR peak and also HbO dip with that of the simulated HbR of balloon model can be observed (Table 5.2). tHb decreases slowly as in balloon model CBV.

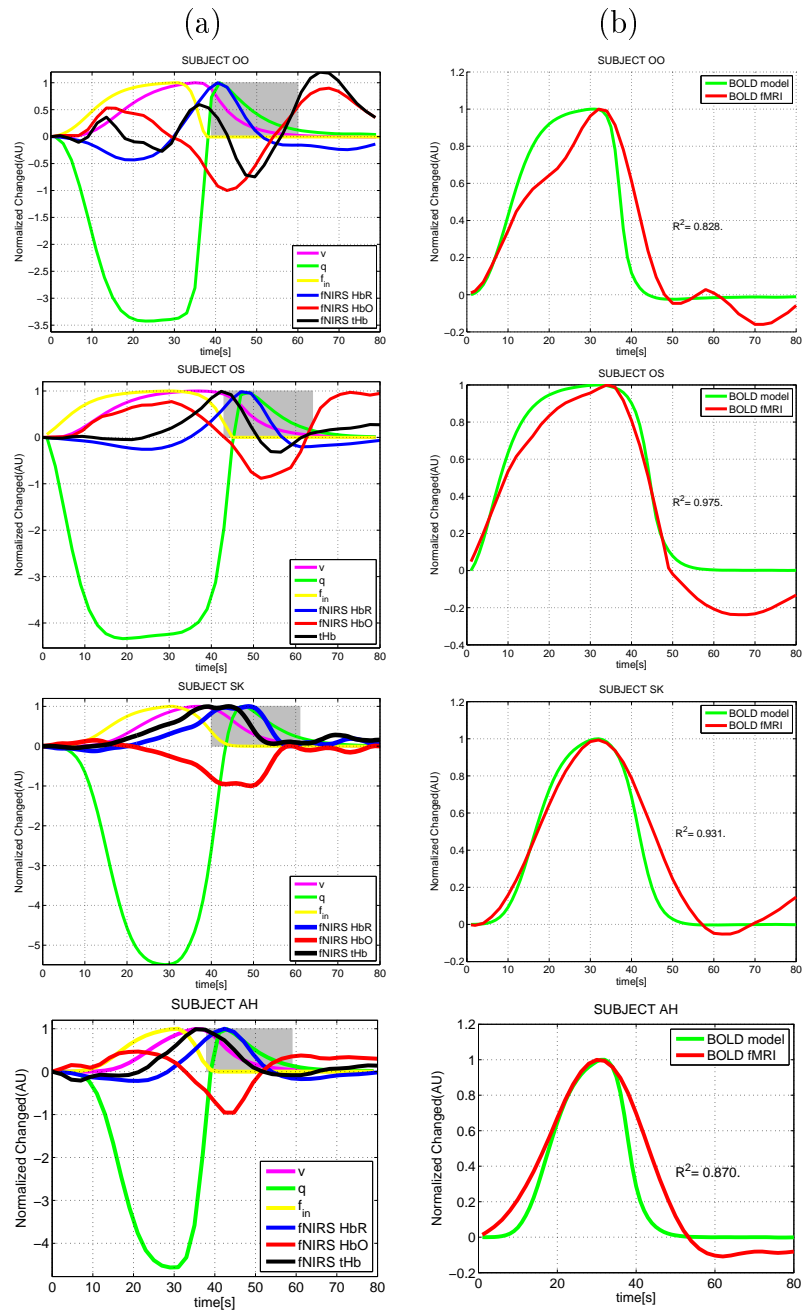


Figure 5.6 (a) Average time course of fNIRS derived HbR data and balloon model outputs for q (identical to HbR), f_{in} (identical to CBF) and v (identical to CBV). Shaded areas represent the post stimulus undershoot duration. (b) average time course of BOLD signal measured from fMRI and derived balloon model BOLD signal. Model parameters were $\alpha = 0.38$, $V_0 = 0.02$, $\tau_0 = 3$ s, $\tau_+ = 0$, $\tau_- = 13$, $E_0 = 0.1$.

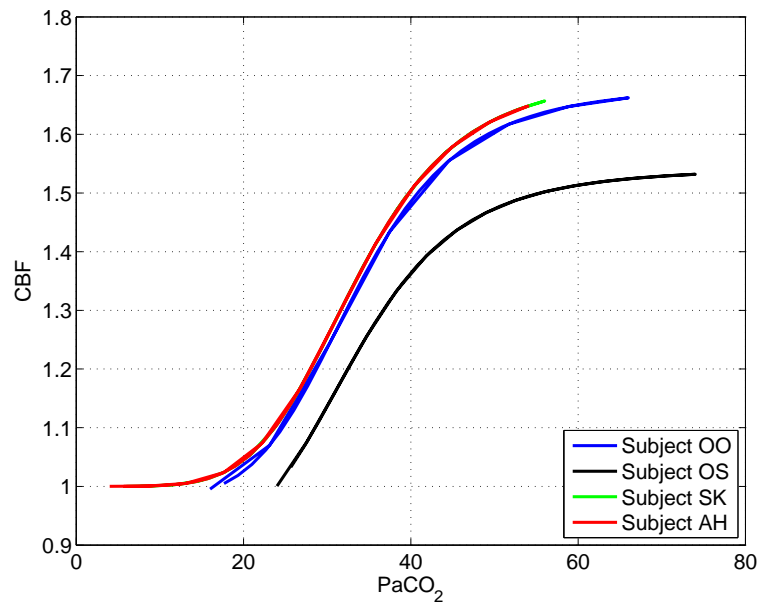


Figure 5.7 Cerebral blood flow (CBF) as a function of PaCO_2 . Graphs obtained from the best fit parameters (Table 5.3) of the Eq. 5.1 used in Figure 5.6.

We used simulated PaCO_2 change to drive the balloon model according to changes during breath hold by Eq. 5.1. Figure 5.7 illustrates CBF- PaCO_2 relationship of each subject which provides the best BOLD and fNIRS HbR-HbO fit parameters (Table 3). CBF- PaCO_2 of two subjects (SK and AH) are similar. Their initial PaCO_2 values are between 5-10 mmHg. On the other hand, PaCO_2 values in the remaining two subjects (OO and OS) are different, 15-25 mmHg. The CBF- PaCO_2 relationship curve for subject OS is shifted slightly to the right in comparison to the other three.

Table 5.3

Sigmoidal function parameters in Eq. 5.1 which describe relation between CBF and PaCO_2 (Figure 5.6).

Subjects	a	b	c
OO	0.6307	0.236	33.49
OS	0.7557	0.1308	30.53
SK	0.6485	0.1877	32.77
AH	0.6508	0.1899	32.85

6. Discussion

6.0.1 Effects of Breath Hold on Cerebral Hemodynamics

During neuronal activity, CBF status can be changed metabolically by vasodilatory agents, such as CO_2 , H^+ , K^+ and NO [14]. Therefore, as one of the major products of cerebral metabolism, CO_2 can alter CBF by effecting VMR of the cerebral vasculature. This mechanism is mediated mainly through the influence of increased CO_2 levels on the central chemoreceptor of the brain stem. CO_2 diffuses easily from the blood into the cerebrospinal fluid, where it is hydrated and forms carbonic acid. As the acid dissociates, hydrogen ions are released and the pH of cerebrospinal fluid drops [22]. This leads to smooth muscle relaxation of the arteries resulting in vasodilation and ultimately an increase in CBF. Effects of CO_2 on cerebrovascular dynamics and therefore CBF have been studied extensively. It has been shown that 5- 7 % CO_2 inhalation in humans produces an increase in CBF averaging 75 % [103]. Similar results were also observed in animals. Raising the PaCO_2 level from 40 to 80 mmHg caused a 100 % increase in CBF [110]. In addition to this, Sage et al. (1981) [156] measured a significant increase in CBF as the rats inspired CO_2 . Similar to CO_2 inhalation task, a 28-30s BHT in humans induces a comparable hypercapnic situation which was observed to be at least as effective as the 5 % CO_2 method [141, 147]. Several others have investigated the cerebrovascular reactivity to BHT extensively with BOLD fMRI. Stillman et al. (1995) [158] and Moritz et al. (1998) [159] have reported 3-10 % BOLD change. Kwong et al. (1995) [160] and Kastrup et al. (1998) [161] demonstrated 3.2 % and 0.8-3.5 % BOLD change respectively.

In this study, we chose not to measure PaCO_2 due to its invasiveness but assume a hypothetical waveshape as the driving function of the EBM. An indirect method, endtidal CO_2 ($P_{ET}\text{CO}_2$) measurements, a non-invasive technique for estimating PaCO_2 , does not reflect accurately PaCO_2 when hemodynamics are unsteady such as during BHT [162, 163, 164, 165]. Our choice on PaCO_2 is similar to the one of the original

Balloon Model paper [1] where they have not measured CBF but instead assumed a hypothetical waveshape. Similarly in a recent study by Obata et al, a hypothetical CMRO₂ waveshape was assumed as a driving function of the balloon model [32].

In this study, we utilized a customized sigmoidal function for each subject to characterize the relationship between PaCO₂ and CBF during BHT and used this function as the driving function to the balloon model. The fNIRS and fMRI data were fit to this new model to estimate the parameters of the model for each subject. One of the significant results of this customization is that our data show an inverse relationship between the amplitude of BOLD percent change and the PaCO₂ baseline level obtained from the model (Figure 6.1). Subject OS with lowest BOLD response, 0.4 % had the highest initial PaCO₂, 25.6 mmHg, whereas subject SK with highest BOLD, 2.2 %, response had the lowest initial PaCO₂ level, 7.7 mmHg. This is in agreement with the previous studies [104, 146, 155], where it was demonstrated that a reduction in BOLD response occurs after the use of vasodilatory agents. In direct contrast, there are several studies which suggest that absolute BOLD signal change is not effected by the baseline PaCO₂ level [157, 166, 91, 167]. Baseline changes have an additive effect on BOLD percentage change. The result of Posse et al. (2001) [166] study was different because they observed a reduction at higher CO₂ levels. Further multimodal studies could settle this contentious issue.

6.0.2 BOLD and fNIRs Vasoreactivity Transients During Breath Hold

Figure 5.6 reports time series of four subjects during BHT. Two main VMR transients are observed on the time series of both fNIRS and BOLD data.

VMR transient 1 (during BHT), in which CBF increase dominates all hemodynamic responses. As pointed above VMR due to the BHT increases the CBF. By increasing the CBF, much oxygenated blood with a reduction in oxygen extraction in a region of brain provides an increase in local fNIRS HbO and a decrease in local fNIRS HbR. Transient 1 is the best identified part of BHT [141, 168, 143]. Uncou-

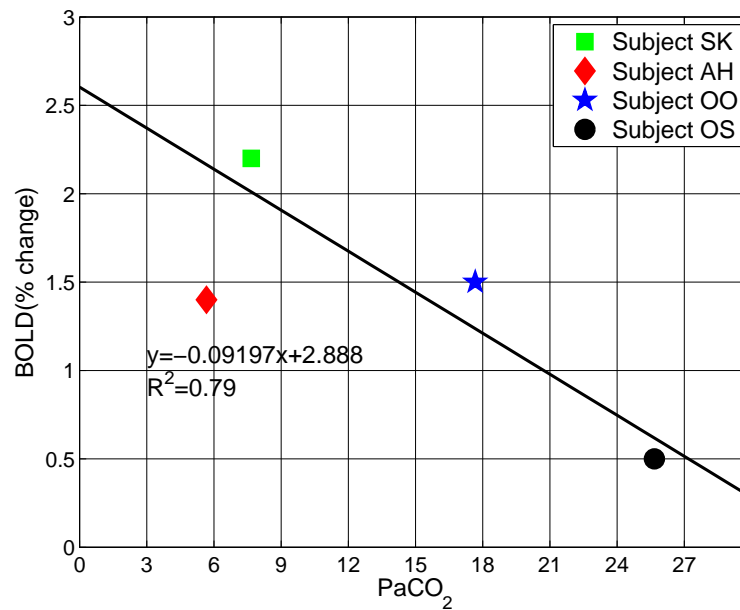


Figure 6.1 The relationship of BOLD signal change on the baseline level of PaCO₂. Individual data point indicates different subject.

pling between oxygen utilization and CBF is hypothesized to be responsible for the major peaking of the BOLD and fNIRS HbO signal during BHT. According to these, it is expected that fNIRS HbO will increase due to the blood flow increase to reduce hypercapnic effect till the end of the breath hold episode.

VMR transient 2 (end of BHT), in which when the VMR has already reached its maximum and starts to decrease to baseline level. fNIRS observation shows that this transient can be characterized by a decrease of fNIRS HbO and a progressive increase of the fNIRS HbR level. Within this interval BOLD signal exhibits post stimulus undershoot or remain constant. These findings are also in agreement with the previous fNIRS and fMRI studies. Recent studies done with fNIRS have reported a progressive HbR increase at the end of the BHT [169, 170, 133, 132]. Moreover, MacIntosh et al. (2003) [129] and Hulvershorn et al. (2003) [130] reported an increase in HbR mirrored the post stimulus undershoot in the BOLD. It has been suggested that post stimulus undershoot is caused by elevated CBV that returns to baseline more slowly than CBF [1] or by a continued elevation of CMRO₂ following the end of stimulus [97] or by dropped CBF below the baseline [93].

BHT and CO₂ challenge is a widespread method for testing the VMR [135, 170, 133, 132, 171, 139, 104, 141, 138, 107, 147, 100, 103]. However, one point of criticism of these results is the unknown influence of the extracerebral tissue on cerebral fNIRS signal. Theoretically, the fNIRS signal is considered to originate from a banana-shaped volume starting from the superficial layers (skin and extracranial tissue) and extending to deeper cortical layers. Hence, contributions from the superficial layers, cannot be completely ruled out [172, 173, 124]. Generally, it has been considered that source detector distances could decrease to 2-2.5 cm, where gray matter is part of the sampled volume [148, 149, 150, 116, 151]. Recent findings of Kato et al. [149] also support this. In addition, previous work has shown that changes in fNIRS data due to mild hypercapnia challenges did not result in extracerebral perfusion changes such as scalp effects [174]. Furthermore, Grubhofer et al. (1997) [175] found that there was no correlation between fNIRS measurements and facial vein. Macintosh et al. [129] et al suggested that BHT task is suitable for comparing fMRI and NIRS measurements. As we expected, and contrary to influence of the extracerebral tissue, we observed an increase in HbO and a decrease in HbR within the first 10-20s.

In Figure 5.6, there are differences between EBM parameters (q, v) and fNIRS measured HbR-tHb signal. This needs to be explored further. An explanation for this was proposed by the different compartmental sensitivity characteristics regarding to the vessel diameter between two modalities [3, 149]. Gradient echo (GE) sequence mostly used in fMRI studies is sensitive to vessel larger than 10 μm . The diffusion weighted (DW) EPI studies which suppress intravascular signal while preserving extravascular and microvascular signals are consistent with our results since post stimulus was not affected by diffusion gradients where BOLD peak was attenuated. This post stimulus effect was explained as a result of slow resolving of CBV [33, 37, 36, 34]. In addition, fNIRS is known to be sensitive to micro vascular space since photons entering the large vessels have but very low probability to escape the larger absorber [3, 149]. Our data suggest that HbR and CBV's temporal behavior of the model and fNIRS HbR and tHb coincide during the post stimulus undershoot since observed and derived peaks of the transients are very close (Table 5.2). In Figure 5.6(a), it can be seen that there is a temporal lag between CBF and CBV return to baseline producing the post stimulus

undershoot of the BOLD signal. This is also supported by the tHB measurement of the fNIRS. Recently published paper [169] which suggests delayed initial cerebral vasodilation as an explanation for HbR increase at the end of BHT also supports our findings.

7. Conclusion

This dissertation research demonstrates an expanded application of balloon model which has been mentioned as a needed research for combined fNIRS-fMRI experiments in a recently published review article (see Table 1 in Steinbrink et al. (2000) [3]). Results of PaCO₂ EBM suggest that initial levels of vasodilatory agent (PaCO₂ in this study) affect the baseline level of CBF, therefore the BOLD signal. Since basal CBF varies in different brain regions due to these agents, it is difficult to compare BOLD responses across these regions. Furthermore, our study explores for the first time the post stimulus undershoot during BHT using balloon model in a combined fMRI-fNIRS study. Results suggest that post stimulus undershoot measured by fMRI is dominated by slow return of CBV which is supported by fNIRS measurements and EBM simulations. The biophysical interpretation of fMRI-fNIRS measurements framework presented here by integrating PaCO₂ changes to balloon model should be useful not only in cognitive tasks by estimating basal level of CBF but also understanding the intricate dynamics of CBV, CMRO₂ and HbR concentration. We believe, integration of technologies, fMRI and fNIRS, and their combined analysis with biophysical models will be the cornerstone for the future neuroimaging studies aiming to dissect the underlying physiological principles and dynamics of neurovascular response.

This dissertation research has focused on the underlying physiology of BOLD signal in human brain using different modalities and modeling method. The BOLD signal is measure of local variations in hemoglobin concentration changes that are determined by a combination of CBF, CBV, CMRO₂. We now know much about the physiological basis of BOLD signal transients, positive BOLD and post stimulus undershoot during breath holding. Although much is known about physiological basis, how local CBF, CMRO₂ and PaCO₂ are changed qualitatively/quantitatively is an unanswered question. This would be a future direction of investigation. Building up a new experimental setup that can simultaneously monitor, CBF using ASL sequence, CMRO₂ using fNIRS and PaCO₂ during BHT or cognitive task will help in under-

standing the coupling physiology and neuronal activity.

APPENDIX A. Published Papers During the PhD Studies

Parts of the work presented in this thesis have been published in the form of seven conference articles and two journal articles. These publications are listed in the following subsections.

A.1 Journal Papers

1. Emir, U. E., C. Ozturk, and A. Akin, “Multimodal investigation of fmri and fnirs derived breath hold bold signals with an expanded balloon model”, *Physiol Meas*, Vol. 29, pp. 49-63, 2008.
2. Akin, A., D. Bilensoy, U. E. Emir, M. Glsoy, S. Candansayar, and H. Bolay, “Cerebrovascular dynamics in patients with migraine: near-infrared spectroscopy study., *Neurosci Lett*, Vol. 400, pp. 86-91, May 2006.

A.2 Conference Proceedings

1. Emir, U. E., O. Sayli, K. Aydin, C. Ozturk, A. Ademoglu, and A. Akin, “Investigating fmri and fnirs signal with balloon model during breath hold task”, in *Proc Int Soc for Magn Reson in Med*, 2007.
2. Emir, U. E., A. D. Duru, A. Ademoglu, and A. Akin, “Coregistration of fnirs data on to the realistic head model.”, *Conf Proc IEEE Eng Med Biol Soc*, Vol. 3, pp. 3184-3187, 2005.
3. Emir, U. E., S. Kalsin, O. Sayli, C. Ozturk, and A. Akin, “Design of an mr compatible fnirs instrument”, in *Photonics West*, 2005.
4. Emir, U. E., D. Bilensoy, and A. Akin, “fnirs measurements in migraine”, in *Photonics West*, 2005.

5. Emir, U. E., O. Sayli, and A. Akin, "Frequency components in breath holding experiments", in Photonics West, 2005.
6. Akin, A., U. Emir, and H. Bolay, "Cerebral hemodynamic reactivity measured by near infrared spectroscopy in migraineurs"., Conf Proc IEEE Eng Med Biol Soc, Vol. 2, no. 1, pp. 1484-1487, 2005.
7. Emir, U. E., O. Sayli, K. Aydin, C. Ozturk, A. Ademoglu, and A. Akin, "Effect of repetitive breathholding on bold and fnirs signals", in Conf Proc BMES 2004 Fall Meeting, 2004.

REFERENCES

1. Buxton, R. B., E. C. Wong, and L. R. Frank, "Dynamics of blood flow and oxygenation changes during brain activation: the balloon model.," *Magn Reson Med*, Vol. 39, pp. 855–864, Jun 1998.
2. Buxton, R. B., K. Uludag, D. J. Dubowitz, and T. T. Liu, "Modeling the hemodynamic response to brain activation," *NeuroImage*, Vol. 23, pp. S220–S233, 2004.
3. Steinbrink, J., A. Villringer, F. Kempf, D. Haux, S. Boden, and H. Obrig, "Illuminating the bold signal: combined fmri-fnirs studies.," *Magn Reson Imaging*, Vol. 24, pp. 495–505, May 2006.
4. Silverthorn, D. U., *Human Physiology*, Prentice-Hall, 2001.
5. Pellerin, L., and P. J. Magistretti, "Food for thought: challenging the dogmas.," *J Cereb Blood Flow Metab*, Vol. 23, pp. 1282–1286, Nov 2003.
6. Clarke, D. D., and L. Sokoloff, *Circulation and energy metabolism of the brain*, no. 645–680, 5th ed., 1994.
7. Magistretti, P. J., L. Pellerin, D. L. Rothman, and R. G. Shulman, "Energy on demand.," *Science*, Vol. 283, pp. 496–497, Jan 1999.
8. Attwell, D., and S. B. Laughlin, "An energy budget for signaling in the grey matter of the brain.," *J Cereb Blood Flow Metab*, Vol. 21, pp. 1133–1145, Oct 2001.
9. Tsacopoulos, M., and P. J. Magistretti, "Metabolic coupling between glia and neurons.," *J Neurosci*, Vol. 16, pp. 877–885, Feb 1996.
10. Magistretti, P. J., and L. Pellerin, "The contribution of astrocytes to the 18f-2-deoxyglucose signal in pet activation studies.," *Mol Psychiatry*, Vol. 1, pp. 445–452, Dec 1996.
11. Magistretti, P. J., and L. Pellerin, "Cellular mechanisms of brain energy metabolism. relevance to functional brain imaging and to neurodegenerative disorders.," *Ann N Y Acad Sci*, Vol. 777, pp. 380–387, Jan 1996.
12. Magistretti, P. J., and L. Pellerin, "Cellular bases of brain energy metabolism and their relevance to functional brain imaging: evidence for a prominent role of astrocytes.," *Cereb Cortex*, Vol. 6, no. 1, pp. 50–61, 1996.
13. Magistretti, P. J., and L. Pellerin, "Cellular mechanisms of brain energy metabolism and their relevance to functional brain imaging.," *Philos Trans R Soc Lond B Biol Sci*, Vol. 354, pp. 1155–1163, Jul 1999.
14. Buxton, R. B., *Introduction to Functional Magnetic Resonance Imaging*, Cambridge, 2002.
15. Lauritzen, M., and L. Gold, "Brain function and neurophysiological correlates of signals used in functional neuroimaging.," *J Neurosci*, Vol. 23, pp. 3972–3980, May 2003.
16. Logothetis, N. K., J. Pauls, M. Augath, T. Trinath, and A. Oeltermann, "Neurophysiological investigation of the basis of the fmri signal.," *Nature*, Vol. 412, pp. 150–157, Jul 2001.

17. Logothetis, N. K., "The underpinnings of the bold functional magnetic resonance imaging signal.," *J Neurosci*, Vol. 23, pp. 3963–3971, May 2003.
18. Shmuel, A., M. Augath, A. Oeltermann, and N. K. Logothetis, "Negative functional mri response correlates with decreases in neuronal activity in monkey visual area v1.," *Nat Neurosci*, Vol. 9, pp. 569–577, Apr 2006.
19. Moonen, C. T. W., and P. A. Bandettini, *Functional MRI*, Springer, 2000.
20. Attwell, D., and C. Iadecola, "The neural basis of functional brain imaging signals.," *Trends Neurosci*, Vol. 25, pp. 621–625, Dec 2002.
21. Walters, F. J., "Neuro anaesthesia—a review of the basic principles and current practices.," *Cent Afr J Med*, Vol. 36, pp. 44–51, Feb 1990.
22. Madden, J. A., "The effect of carbon dioxide on cerebral arteries.," *Pharmacol Ther*, Vol. 59, pp. 229–250, Aug 1993.
23. Kontos, H. A., E. P. Wei, A. J. Raper, and J. L. Patterson, "Local mechanism of co2 action of cat pial arterioles.," *Stroke*, Vol. 8, no. 2, pp. 226–229, 1977.
24. Kontos, H. A., A. J. Raper, and J. L. Patterson, "Analysis of vasoactivity of local ph, pco2 and bicarbonate on pial vessels.," *Stroke*, Vol. 8, no. 3, pp. 358–360, 1977.
25. Gotoh, F., Y. Tazaki, and J. S. Meyer, "Transport of gases through brain and their extravascular vasomotor action.," *Exp Neurol*, Vol. 4, pp. 48–58, Jul 1961.
26. Amano, T., "A brief review of dr f gotoh's contribution to neuroscience: research in the field of cerebral blood flow and stroke.," *Keio J Med*, Vol. 50, pp. 72–80, Jun 2001.
27. Weisskoff, R. M., and S. Kiihne, "Mri susceptometry: image-based measurement of absolute susceptibility of mr contrast agents and human blood.," *Magn Reson Med*, Vol. 24, pp. 375–383, Apr 1992.
28. Thulborn, K. R., J. C. Waterton, P. M. Matthews, and G. K. Radda, "Oxygenation Dependence of the Transverse Relaxation Time of Water Protons in Whole Blood at High Field.," *Biochem. Biophys. Acta.*, Vol. 714, pp. 265–270, 1982.
29. Chu, S. C. K., Y. Xu, J. A. Balschi, and C. S. Springer, "Bulk Magnetic Susceptibility Shifts in NMR Studies of Compartmentalized Samples: Use of Paramagnetic Reagents.," *Magn. Reson. Med.*, Vol. 13, pp. 239–262, 1990.
30. Spees, W. M., D. A. Yablonskiy, M. C. Oswood, and J. J. Ackerman, "Water proton mr properties of human blood at 1.5 tesla: magnetic susceptibility, $t(1)$, $t(2)$, $t^*(2)$, and non-lorentzian signal behavior.," *Magn Reson Med*, Vol. 45, pp. 533–542, Apr 2001.
31. Bandettini, P. A., *Magnetic resonance imaging of human brain activation using endogenous susceptibility contrast*. PhD thesis, Faculty of the graduate school of the medical college of wisconsin, 1994.
32. Obata, T., T. T. Liu, K. L. Miller, W. M. Luh, E. C. Wong, L. R. Frank, and R. B. Buxton, "Discrepancies between bold and flow dynamics in primary and supplementary motor areas: application of the balloon model to the interpretation of bold transients.," *Neuroimage*, Vol. 21, pp. 144–153, Jan 2004.

33. Boxerman, J. L., P. A. Bandettini, K. K. Kwong, J. R. Baker, T. L. Davis, B. R. Rosen, and R. M. Weisskoff, "The intravascular contribution to fmri signal change: Monte carlo modeling and diffusion-weighted studies in vivo.," *Magn Reson Med*, Vol. 34, pp. 4–10, Jul 1995.
34. Song, A. W., E. C. Wong, S. G. Tan, and J. S. Hyde, "Diffusion weighted fmri at 1.5 t.," *Magn Reson Med*, Vol. 35, pp. 155–158, Feb 1996.
35. Buxton, R. B., W.-M. Luh, E. C. Wong, L. R. Frank, and P. A. Bandettini, "Diffusion-Weighted Attenuates the BOLD Peak Signal Change But not the Post-Stimulus Under-shoot," in *ISMRM*, 1998.
36. Song, A. W., H. Fichtenholtz, and M. Woldorff, "Bold signal compartmentalization based on the apparent diffusion coefficient.," *Magn Reson Imaging*, Vol. 20, pp. 521–525, Sep 2002.
37. Menon, R. S., "Postacquisition suppression of large-vessel bold signals in high-resolution fmri.," *Magn Reson Med*, Vol. 47, pp. 1–9, Jan 2002.
38. Edelman, R. R., B. Siewert, D. G. Darby, V. Thangaraj, A. C. Nobre, M. M. Mesulam, and S. Warach, "Qualitative mapping of cerebral blood flow and functional localization with echo-planar mr imaging and signal targeting with alternating radio frequency.," *Radiology*, Vol. 192, pp. 513–520, Aug 1994.
39. Edelman, R. R., and Q. Chen, "Epistar mri: multislice mapping of cerebral blood flow.," *Magn Reson Med*, Vol. 40, pp. 800–805, Dec 1998.
40. Luh, W. M., E. C. Wong, P. A. Bandettini, and J. S. Hyde, "Quipss ii with thin-slice til periodic saturation: a method for improving accuracy of quantitative perfusion imaging using pulsed arterial spin labeling.," *Magn Reson Med*, Vol. 41, pp. 1246–1254, Jun 1999.
41. Wong, E. C., W. M. Luh, and T. T. Liu, "Turbo asl: arterial spin labeling with higher snr and temporal resolution.," *Magn Reson Med*, Vol. 44, pp. 511–515, Oct 2000.
42. Tuunanen, P. I., and R. A. Kauppinen, "Effects of Oxygen Saturation on BOLD and Arterial Spin Labeling Perfusion fMRI signals Studied in a Motor Activation Task.," *NeuroImage*, Vol. 20, pp. 102–109, 2006.
43. Ogawa, S., R. S. Menon, D. W. Tank, S. G. Kim, H. Merkle, J. M. Ellermann, and K. Ugurbil, "Functional brain mapping by blood oxygenation level-dependent contrast magnetic resonance imaging. a comparison of signal characteristics with a biophysical model.," *Biophys J*, Vol. 64, pp. 803–812, Mar 1993.
44. Bernstein, M. A., K. F. King, and X. J. Zhou, *Handbook of MRI Pulse Sequences*, Elsevier, 2004.
45. Chance, B., M. Cope, E. Gratton, N. Ramanujam, and B. Tromberg, "Phase Measurement Absorption and Scatter in Human Tissue," *Rev. Sci. Instru.*, Vol. 69, pp. 3457–3481, 1998.
46. Coyle, S., *Near-infrared spectroscopy for brain computer interfacing*. PhD thesis, Maynooth Department Of Electronic Engineering, National University Of Ireland,, 2005.
47. Tuchin, V., *Tissue Optics*, Spie Press, 2000.

48. Cope., M., *The application of near-infrared spectroscopy to non-invasive monitoring of cerebral oxygenation in the newborn infant*. PhD thesis, University College London, 1991.
49. Fisher, J. C., "Photons, psychiatrics, and physicians: a practical guide to understanding laser light interaction with living tissue, part i.," *J Clin Laser Med Surg*, Vol. 10, pp. 419–426, Dec 1992.
50. Arnfield, M. R., J. Tulip, and M. S. McPhee, "Optical propagation in tissue with anisotropic scattering.," *IEEE Trans Biomed Eng*, Vol. 35, pp. 372–381, May 1988.
51. Fukui, Y., Y. Ajichi, and E. Okada, "Monte carlo prediction of near-infrared light propagation in realistic adult and neonatal head models.," *Appl Opt*, Vol. 42, pp. 2881–2887, Jun 2003.
52. Okada, E., and D. T. Delpy, "Near-infrared light propagation in an adult head model. ii. effect of superficial tissue thickness on the sensitivity of the near-infrared spectroscopy signal.," *Appl Opt*, Vol. 42, pp. 2915–2922, Jun 2003.
53. Okada, Y., *Biomagnetism: an Interdisciplinary Approach*, ch. Neurogenesis of evoked magnetic fields., pp. 399–408. Plenum Press, 1983.
54. George, J. S., C. J. Aine, J. C. Mosher, D. M. Schmidt, D. M. Ranken, H. A. Schlitt, C. C. Wood, J. D. Lewine, J. A. Sanders, and J. W. Belliveau, "Mapping function in the human brain with magnetoencephalography, anatomical magnetic resonance imaging, and functional magnetic resonance imaging.," *J Clin Neurophysiol*, Vol. 12, pp. 406–431, Sep 1995.
55. Simpson, G. V., M. E. Pflieger, J. J. Foxe, S. P. Ahlfors, H. G. Vaughan, J. Hrabe, R. J. Ilmoniemi, and G. Lantos, "Dynamic neuroimaging of brain function.," *J Clin Neurophysiol*, Vol. 12, pp. 432–449, Sep 1995.
56. Lammertsma, A. A., and R. S. Frackowiak, "Positron emission tomography.," *Crit Rev Biomed Eng*, Vol. 13, no. 2, pp. 125–169, 1985.
57. Toyama, H., M. Ichise, J.-S. Liow, K. J. Modell, D. C. Vines, T. Esaki, M. Cook, J. Seidel, L. Sokoloff, M. V. Green, and R. B. Innis, "Absolute quantification of regional cerebral glucose utilization in mice by 18f-fdg small animal pet scanning and 2-14c-dg autoradiography.," *J Nucl Med*, Vol. 45, pp. 1398–1405, Aug 2004.
58. Bednarczyk, E. M., B. Remler, C. Weikart, A. D. Nelson, and R. C. Reed, "Global cerebral blood flow, blood volume, and oxygen metabolism in patients with migraine headache.," *Neurology*, Vol. 50, pp. 1736–1740, Jun 1998.
59. Kuikka, J. T., J. W. Belliveau, and R. Hari, "Future of functional brain imaging.," *Eur J Nucl Med*, Vol. 23, pp. 737–740, Jul 1996.
60. Matthews, P. M., *Functional mri: an introduction to methods*, ch. An introduction to functional magnetic resonance imaging of the brain, pp. 3–35. Oxford University Press, 2001.
61. Ritter, P., and A. Villringer, "Simultaneous eeg-fmri.," *Neurosci Biobehav Rev*, Vol. 30, no. 6, pp. 823–838, 2006.

62. Moosmann, M., P. Ritter, I. Krastel, A. Brink, S. Thees, F. Blankenburg, B. Taskin, H. Obrig, and A. Villringer, "Correlates of alpha rhythm in functional magnetic resonance imaging and near infrared spectroscopy.," *Neuroimage*, Vol. 20, pp. 145–158, Sep 2003.
63. Guy, C. N., D. H. Ffytche, A. Brovelli, and J. Chumillas, "fMRI and EEG Responses to Periodic Visual Stimulation," *NeuroImage*, Vol. 10, pp. 125–148, 1999.
64. Singh, M., S. Kim, and T.-S. Kim, "Correlation between bold-fmri and eeg signal changes in response to visual stimulus frequency in humans.," *Magn Reson Med*, Vol. 49, pp. 108–114, Jan 2003.
65. Wan, X., J. Riera, K. Iwata, M. Takahashi, T. Wakabayashi, and R. Kawashima, "The neural basis of the hemodynamic response nonlinearity in human primary visual cortex: Implications for neurovascular coupling mechanism.," *Neuroimage*, Vol. 32, pp. 616–625, Aug 2006.
66. Pastor, M. A., J. Artieda, J. Arbizu, M. Valencia, and J. C. Masdeu, "Human cerebral activation during steady-state visual-evoked responses.," *J Neurosci*, Vol. 23, pp. 11621–11627, Dec 2003.
67. Sotero, R. C., and N. J. Trujillo-Barreto, "Biophysical model for integrating neuronal activity, eeg, fmri and metabolism.," *Neuroimage*, Vol. 39, pp. 290–309, January 2008.
68. Laufs, H., A. Kleinschmidt, A. Beyerle, E. Eger, A. Salek-Haddadi, C. Preibisch, and K. Krakow, "Eeg-correlated fmri of human alpha activity.," *Neuroimage*, Vol. 19, pp. 1463–1476, Aug 2003.
69. Newberg, A. B., J. Wang, H. Rao, R. L. Swanson, N. Wintering, J. S. Karp, A. Alavi, J. H. Greenberg, and J. A. Detre, "Concurrent cbf and cmrglc changes during human brain activation by combined fmri-pet scanning.," *Neuroimage*, Vol. 28, pp. 500–506, Nov 2005.
70. Yang, Y., H. Gu, and E. A. Stein, "Simultaneous mri acquisition of blood volume, blood flow, and blood oxygenation information during brain activation.," *Magn Reson Med*, Vol. 52, pp. 1407–1417, Dec 2004.
71. Gu, H., E. A. Stein, and Y. Yang, "Nonlinear responses of cerebral blood volume, blood flow and blood oxygenation signals during visual stimulation.," *Magn Reson Imaging*, Vol. 23, pp. 921–928, Nov 2005.
72. Liu, H. L., Y. Pu, L. D. Nickerson, Y. Liu, P. T. Fox, and J. H. Gao, "Comparison of the temporal response in perfusion and bold-based event-related functional mri.," *Magn Reson Med*, Vol. 43, pp. 768–772, May 2000.
73. Yongbi, M. N., F. Fera, Y. Yang, J. A. Frank, and J. H. Duyn, "Pulsed arterial spin labeling: comparison of multisection baseline and functional mr imaging perfusion signal at 1.5 and 3.0 t: initial results in six subjects.," *Radiology*, Vol. 222, pp. 569–575, Feb 2002.
74. Detre, J. A., and J. Wang, "Technical aspects and utility of fmri using bold and asl.," *Clin Neurophysiol*, Vol. 113, pp. 621–634, May 2002.
75. Chiarelli, P. A., D. P. Bulte, D. Gallichan, S. K. Piechnik, R. Wise, and P. Jezzard, "Flow-metabolism coupling in human visual, motor, and supplementary motor areas assessed by magnetic resonance imaging.," *Magn Reson Med*, Vol. 57, pp. 538–547, Mar 2007.

76. Strangman, G., J. P. Culver, J. H. Thompson, and D. A. Boas, "A quantitative comparison of simultaneous bold fmri and nirs recordings during functional brain activation.," *Neuroimage*, Vol. 17, pp. 719–731, Oct 2002.
77. Toronov, V. Y., X. Zhang, and A. G. Webb, "A spatial and temporal comparison of hemodynamic signals measured using optical and functional magnetic resonance imaging during activation in the human primary visual cortex.," *Neuroimage*, Vol. 34, pp. 1136–1148, Feb 2007.
78. Chen, Y., D. R. Taylor, X. Intes, and B. Chance, "Correlation between near-infrared spectroscopy and magnetic resonance imaging of rat brain oxygenation modulation.," *Phys Med Biol*, Vol. 48, pp. 417–427, Feb 2003.
79. Siegel, A. M., J. P. Culver, J. B. Mandeville, and D. A. Boas, "Temporal comparison of functional brain imaging with diffuse optical tomography and fmri during rat forepaw stimulation.," *Phys Med Biol*, Vol. 48, pp. 1391–1403, May 2003.
80. Boas, D. A., G. Strangman, J. P. Culver, R. D. Hoge, G. Jaszewski, R. A. Poldrack, B. R. Rosen, and J. B. Mandeville, "Can the cerebral metabolic rate of oxygen be estimated with near-infrared spectroscopy?," *Phys Med Biol*, Vol. 48, pp. 2405–2418, Aug 2003.
81. Mandeville, J. B., J. J. Marota, C. Ayata, M. A. Moskowitz, R. M. Weisskoff, and B. R. Rosen, "Mri measurement of the temporal evolution of relative cmro(2) during rat forepaw stimulation.," *Magn Reson Med*, Vol. 42, pp. 944–951, Nov 1999.
82. Ogawa, S., D. W. Tank, R. S. Menon, J. M. Ellerman, S.-G. Kim, and K. Ugurbil, "Intrinsic Signal Changes Accompanying Sensory Stimulation: Functional Brain Mapping with Magnetic Resonance Imaging," *Proc. Natl. Acad. Sci.*, Vol. 89, pp. 5951–5955, 1992.
83. Bandettini, P. A., E. C. Wong, R. S. Hinks, R. S. Tikofsky, and J. S. Hyde, "Time course epi of human brain function during task activation.," *Magn Reson Med*, Vol. 25, pp. 390–397, Jun 1992.
84. Kwong, K. K., J. W. Belliveau, D. A. Chesler, I. E. Goldberg, R. M. Weisskoff, B. P. Poncelet, D. N. Kennedy, B. E. Hoppel, M. S. Cohen, and R. Turner, "Dynamic magnetic resonance imaging of human brain activity during primary sensory stimulation.," *Proc Natl Acad Sci U S A*, Vol. 89, pp. 5675–5679, Jun 1992.
85. Malonek, D., and A. Grinvald, "Interactions between electrical activity and cortical microcirculation revealed by imaging spectroscopy: implications for functional brain mapping.," *Science*, Vol. 272, pp. 551–554, Apr 1996.
86. Hathout, G. M., B. Varjavand, and R. K. Gopi, "The early response in fmri: a modeling approach.," *Magn Reson Med*, Vol. 41, pp. 550–554, Mar 1999.
87. Fox, P. T., and M. E. Raichle, "Focal physiological uncoupling of cerebral blood flow and oxidative metabolism during somatosensory stimulation in human subjects.," *Proc Natl Acad Sci U S A*, Vol. 83, pp. 1140–1144, Feb 1986.
88. Kohl, M., U. Lindauer, G. Royl, M. Kuhl, L. Gold, A. Villringer, and U. Dirnagl, "Physical model for the spectroscopic analysis of cortical intrinsic optical signals.," *Phys Med Biol*, Vol. 45, pp. 3749–3764, Dec 2000.

89. Kennerley, A. J., J. Berwick, J. Martindale, D. Johnston, N. Papadakis, and J. E. Mayhew, "Concurrent fmri and optical measures for the investigation of the hemodynamic response function.," *Magn Reson Med*, Vol. 54, pp. 354–365, Aug 2005.
90. Mildner, T., D. G. Norris, C. Schwarzbauer, and C. J. Wiggins, "A qualitative test of the balloon model for bold-based mr signal changes at 3t.," *Magn Reson Med*, Vol. 46, pp. 891–899, Nov 2001.
91. Hoge, R. D., J. Atkinson, B. Gill, G. R. Crelier, S. Marrett, and G. B. Pike, "Stimulus-dependent bold and perfusion dynamics in human v1.," *Neuroimage*, Vol. 9, pp. 573–585, Jun 1999.
92. Uludag, K., D. J. Dubowitz, E. J. Yoder, K. Restom, T. T. Liu, and R. B. Buxton, "Coupling of cerebral blood flow and oxygen consumption during physiological activation and deactivation measured with fmri," *Neuroimage*, Vol. 23, pp. 148–155, Sep 2004.
93. Liu, T. T., Y. Behzadi, K. Restom, K. Uludag, K. Lu, G. T. Buracas, D. J. Dubowitz, and R. B. Buxton, "Caffeine alters the temporal dynamics of the visual bold response.," *Neuroimage*, Vol. 23, pp. 1402–1413, Dec 2004.
94. Frahm, J., G. Krger, K. D. Merboldt, and A. Kleinschmidt, "Dynamic uncoupling and recoupling of perfusion and oxidative metabolism during focal brain activation in man.," *Magn Reson Med*, Vol. 35, pp. 143–148, Feb 1996.
95. Krger, G., A. Kleinschmidt, and J. Frahm, "Stimulus dependence of oxygenation-sensitive mri responses to sustained visual activation.," *NMR Biomed*, Vol. 11, pp. 75–79, Apr 1998.
96. Krger, G., P. Fransson, K. D. Merboldt, and J. Frahm, "Does stimulus quality affect the physiologic mri responses to brief visual activation?," *Neuroreport*, Vol. 10, pp. 1277–1281, Apr 1999.
97. Lu, H., X. Golay, J. J. Pekar, and P. C. M. V. Zijl, "Sustained poststimulus elevation in cerebral oxygen utilization after vascular recovery.," *J Cereb Blood Flow Metab*, Vol. 24, pp. 764–770, Jul 2004.
98. Grubb, R. L., "the effect of changes in paCo2 on Cerebral Blood Volume, Blood Flow and Vascular Mean Transit Time," *Stroke*, Vol. 5, pp. 630–639, 1974.
99. Friston, K. J., A. Mechelli, R. Turner, and C. J. Price, "Nonlinear responses in fmri: the balloon model, volterra kernels, and other hemodynamics.," *Neuroimage*, Vol. 12, pp. 466–477, Oct 2000.
100. Meyer, J. S., F. Gotoh, Y. Takagi, and R. Kakimi, "Cerebral Hemodynamics, Blood Gases, and Electrolytes during Breath-Holding and the Valsalva Maneuver," *Circulation*, Vol. 33, pp. 35–48, 1966.
101. Shapiro, W., A. J. Wasserman, and J. L. Patterson, "Mechanism and Pattern of Human Cerebrovascular Regulation after Rapid Changes in Blood CO2 Tension," *Journal of Clinical Investigation*, Vol. 45, pp. 913–922, 1966.
102. Shapiro, W., A. J. Wasserman, and J. L. Patterson, "Human Cerebrovascular Response Time to Elevation of Arterial Carbon Dioxide," *Arch Neurol*, Vol. 13, pp. 130–138, 1965.

103. Kety, S. S., and C. F. Schmidt, "The effects of altered arterial tensions of carbon dioxide and oxygen on cerebral blood flow and cerebral oxygen consumption of normal young men.," *J Clin Invest*, Vol. 27, pp. 484–492, Jul 1948.
104. Cohen, E. R., K. Ugurbil, and S.-G. Kim, "Effect of basal conditions on the magnitude and dynamics of the blood oxygenation level-dependent fmri response.," *J Cereb Blood Flow Metab*, Vol. 22, pp. 1042–1053, Sep 2002.
105. Kim, S.-G., E. Rostrup, H. B. Larsson, S. Ogawa, , and O. B. Paulson, "Significant Increases of CBF and CMRO2 during Visual Stimulation," in *ISMRM*, 1999.
106. Prinster, A., C. Pierpaoli, R. Turner, and P. Jezzard, "Simultaneous Measurement of ΔR_2 and ΔR_2^* in Cat Brain during Hypoxia and Hypercapnia," *NeuroImage*, Vol. 6, pp. 191–200, 1997.
107. Toft, P. B., H. Leth, H. C. Lou, Q. P. ad B. Peitersen, and O. Henriksen, "Local Vascular CO2 reactivity in the infant brain assed by functional MRI," *Pediatric Radiology*, Vol. 25, pp. 420–424, 1995.
108. Olesen, J., O. B. Paulson, and N. A. Lassen, "Regional cerebral blood flow in man determined by the initial slope of the clearance of intra-arterially injected ^{133}Xe ," *Stroke*, Vol. 2, no. 6, pp. 519–540, 1971.
109. Patel, M. C., M. G. Taylor, S. Kontis, T. S. Padayachee, and R. G. Gosling, "An online technique for estimating cerebral carbon dioxide reactivity.," *J Biomed Eng*, Vol. 12, pp. 316–318, Jul 1990.
110. Harper, A. M., and H. I. Glass, "Effect of alterations in the arterial carbon dioxide tension on the blood flow through the cerebral cortex at normal and low arterial blood pressures.," *J Neurol Neurosurg Psychiatry*, Vol. 28, pp. 449–452, Oct 1965.
111. Ursino, M., P. D. Giammarco, and E. Belardinelli, "A mathematical model of cerebral blood flow chemical regulation—part ii: Reactivity of cerebral vascular bed.," *IEEE Trans Biomed Eng*, Vol. 36, pp. 192–201, Feb 1989.
112. Ursino, M., P. D. Giammarco, and E. Belardinelli, "A mathematical model of cerebral blood flow chemical regulation—part i: Diffusion processes.," *IEEE Trans Biomed Eng*, Vol. 36, pp. 183–191, Feb 1989.
113. Ursino, M., and P. D. Giammarco, "A mathematical model of the relationship between cerebral blood volume and intracranial pressure changes: the generation of plateau waves.," *Ann Biomed Eng*, Vol. 19, no. 1, pp. 15–42, 1991.
114. Lodi, C. A., and M. Ursino, "Hemodynamic effect of cerebral vasospasm in humans: a modeling study.," *Ann Biomed Eng*, Vol. 27, no. 2, pp. 257–273, 1999.
115. Lu, K., J. W. Clark, F. H. Ghorbel, C. S. Robertson, D. L. Ware, J. B. Zwischenberger, and A. Bidani, "Cerebral autoregulation and gas exchange studied using a human cardiopulmonary model.," *Am J Physiol Heart Circ Physiol*, Vol. 286, pp. H584–H601, Feb 2004.
116. Firbank, M., E. Okada, and D. T. Delpy, "A theoretical study of the signal contribution of regions of the adult head to near-infrared spectroscopy studies of visual evoked responses.," *Neuroimage*, Vol. 8, pp. 69–78, Jul 1998.

117. Liu, H., B. Chance, A. H. Hielscher, S. L. Jacques, and F. K. Tittel, "Influence of blood vessels on the measurement of hemoglobin oxygenation as determined by time-resolved reflectance spectroscopy.," *Med Phys*, Vol. 22, pp. 1209–1217, Aug 1995.
118. Boas, D. A., A. M. Dale, and M. A. Franceschini, "Diffuse optical imaging of brain activation: approaches to optimizing image sensitivity, resolution, and accuracy.," *Neuroimage*, Vol. 23 Suppl 1, pp. S275–S288, 2004.
119. Hoshi, Y., "Functional near-infrared optical imaging: utility and limitations in human brain mapping.," *Psychophysiology*, Vol. 40, pp. 511–520, Jul 2003.
120. Villringer, A., and B. Chance, "Non-invasive optical spectroscopy and imaging of human brain function.," *Trends Neurosci*, Vol. 20, pp. 435–442, Oct 1997.
121. Schroeter, M. L., T. Kupka, T. Mildner, K. Uludag, and D. Y. von Cramon, "Investigating the post-stimulus undershoot of the bold signal—a simultaneous fmri and fnirs study.," *Neuroimage*, Vol. 30, pp. 349–358, Apr 2006.
122. Hoge, R. D., M. A. Franceschini, R. J. M. Covolan, T. Huppert, J. B. Mandeville, and D. Boas, "Simultaneous recording of task-induced changes in blood oxygenation, volume, and flow, using diffuse optical imaging and arterial spin labeling mri," *NeuroImage*, Vol. 25, pp. 701–707, 2005.
123. Yamamoto, T., and T. Kato, "Paradoxical correlation between signal in functional magnetic resonance imaging and deoxygenated haemoglobin content in capillaries: a new theoretical explanation.," *Phys Med Biol*, Vol. 47, pp. 1121–1141, Apr 2002.
124. Mehagnoul-Schipper, D. J., B. F. W. van der Kallen, W. N. J. M. Colier, M. C. van der Sluijs, L. J. T. O. van Erning, H. O. M. Thijssen, B. Oeseburg, W. H. L. Hoefnagels, and R. M. M. Jansen, "Simultaneous measurements of cerebral oxygenation changes during brain activation by near-infrared spectroscopy and functional magnetic resonance imaging in healthy young and elderly subjects.," *Hum Brain Mapp*, Vol. 16, pp. 14–23, May 2002.
125. Toronov, V., A. Webb, J. H. Choi, M. Wolf, A. Michalos, E. Gratton, and D. Hueber, "Investigation of human brain hemodynamics by simultaneous near-infrared spectroscopy and functional magnetic resonance imaging.," *Med Phys*, Vol. 28, pp. 521–527, Apr 2001.
126. Obrig, H., R. Wenzel, M. Kohl, S. Horst, P. Wobst, J. Steinbrink, F. Thomas, and A. Villringer, "Near-infrared spectroscopy: does it function in functional activation studies of the adult brain?," *Int J Psychophysiol*, Vol. 35, pp. 125–142, Mar 2000.
127. Kleinschmidt, A., H. Obrig, M. Requardt, K. D. Merboldt, U. Dirnagl, A. Villringer, and J. Frahm, "Simultaneous recording of cerebral blood oxygenation changes during human brain activation by magnetic resonance imaging and near-infrared spectroscopy.," *J Cereb Blood Flow Metab*, Vol. 16, pp. 817–826, Sep 1996.
128. Toronov, V., S. Walker, R. Gupta, J. H. Choi, E. Gratton, D. Hueber, and A. Webb, "The roles of changes in deoxyhemoglobin concentration and regional cerebral blood volume in the fmri bold signal.," *Neuroimage*, Vol. 19, pp. 1521–1531, Aug 2003.
129. MacIntosh, B. J., L. M. Klassen, and R. S. Menon, "Transient hemodynamics during a breath hold challenge in a two part functional imaging study with simultaneous near-infrared spectroscopy in adult humans.," *Neuroimage*, Vol. 20, pp. 1246–1252, Oct 2003.

130. Hulvershorn, J., L. Bloy, J. S. Leigh, and M. A. Elliott, "Continuous wave optical spectroscopic system for use in magnetic resonance imaging scanners for the measurement of changes in hemoglobin oxygenation states in humans," *Review of Scientific Instruments*, Vol. 74, pp. 4150–4157, 2003.
131. Terborg, C., F. Gora, C. Weiller, and J. Richer, "Reduced vasomotor reactivity in cerebral microangiopathy : a study with near-infrared spectroscopy and transcranial doppler sonography.," *Stroke*, Vol. 31, pp. 924–929, Apr 2000.
132. Akin, A., D. Bilensoy, U. E. Emir, M. Glsoy, S. Candansayar, and H. Bolay, "Cerebrovascular dynamics in patients with migraine: near-infrared spectroscopy study.," *Neurosci Lett*, Vol. 400, pp. 86–91, May 2006.
133. Akin, A., and D. Bilensoy, "Cerebrovascular reactivity to hypercapnia in migraine patients measured with near-infrared spectroscopy.," *Brain Res*, Vol. 1107, pp. 206–214, Aug 2006.
134. Silvestrini, M., R. Baruffaldi, M. Bartolini, F. Vernieri, C. Lanciotti, M. Matteis, E. Troisi, and L. Provinciali, "Basilar and middle cerebral artery reactivity in patients with migraine.," *Headache*, Vol. 44, pp. 29–34, Jan 2004.
135. Liboni, W., F. Molinari, G. Allais, O. Mana, E. Negri, G. Grippi, C. Benedetto, G. D'Andrea, and G. Bussone, "Why do we need nirs in migraine?," *Neurol Sci*, Vol. 28 Suppl 2, pp. S222–S224, May 2007.
136. Vernieri, F., F. Tibuzzi, P. Pasqualetti, N. Rosato, F. Passarelli, P. M. Rossini, and M. Silvestrini, "Transcranial doppler and near-infrared spectroscopy can evaluate the hemodynamic effect of carotid artery occlusion.," *Stroke*, Vol. 35, pp. 64–70, Jan 2004.
137. McGown, A. D., H. Makker, C. Elwell, P. G. A. Rawi, A. Valipour, and S. G. Spiro, "Measurement of changes in cytochrome oxidase redox state during obstructive sleep apnea using near-infrared spectroscopy.," *Sleep*, Vol. 26, pp. 710–716, Sep 2003.
138. Hayakawa, T., M. Terashima, Y. Kayukawa, T. Ohta, and T. Okada, "Changes in cerebral oxygenation and hemodynamics during obstructive sleep apneas.," *Chest*, Vol. 109, pp. 916–921, Apr 1996.
139. Safonova, L. P., A. Michalos, U. Wolf, J. H. Choi, M. Wolf, W. W. Mantulin, D. M. Hueber, and E. Gratton, "Diminished cerebral circulatory autoregulation in obstructive sleep apnea investigated by near-infrared spectroscopy," *Sleep Research Online*, Vol. 5(4), pp. 123–132, 2003.
140. Bulte, D. P., P. A. Chiarelli, R. G. Wise, and P. Jezzard, "Cerebral perfusion response to hyperoxia.," *J Cereb Blood Flow Metab*, Vol. 27, pp. 69–75, Jan 2007.
141. Kastrup, A., G. Krger, T. Neumann-Haefelin, and M. E. Moseley, "Assessment of cerebrovascular reactivity with functional magnetic resonance imaging: comparison of co(2) and breath holding.," *Magn Reson Imaging*, Vol. 19, pp. 13–20, Jan 2001.
142. Kastrup, A., G. Krger, G. H. Glover, and M. E. Moseley, "Assessment of cerebral oxidative metabolism with breath holding and fmri.," *Magn Reson Med*, Vol. 42, pp. 608–611, Sep 1999.
143. Li, T. Q., A. Kastrup, A. M. Takahashi, and M. E. Moseley, "Functional mri of human brain during breath holding by bold and fair techniques.," *Neuroimage*, Vol. 9, pp. 243–249, Feb 1999.

144. Kastrup, A., J. Dichgans, M. Niemeier, and M. Schabet, "Changes of cerebrovascular co2 reactivity during normal aging.," *Stroke*, Vol. 29, pp. 1311–1314, Jul 1998.
145. Davis, T. L., K. K. Kwong, R. M. Weisskoff, and B. R. Rosen, "Calibrated functional mri: mapping the dynamics of oxidative metabolism.," *Proc Natl Acad Sci U S A*, Vol. 95, pp. 1834–1839, Feb 1998.
146. Bandettini, P. A., and E. C. Wong, "A hypercapnia-based normalization method for improved spatial localization of human brain activation with fmri.," *NMR Biomed*, Vol. 10, no. 4-5, pp. 197–203, 1997.
147. Markus, H. S., and M. J. Harrison, "Estimation of cerebrovascular reactivity using transcranial doppler, including the use of breath-holding as the vasodilatory stimulus.," *Stroke*, Vol. 23, pp. 668–673, May 1992.
148. Bunce, S. C., M. Izzetoglu, K. Izzetoglu, B. Onaral, and K. Pourrezaei, "Functional near-infrared spectroscopy.," *IEEE Eng Med Biol Mag*, Vol. 25, no. 4, pp. 54–62, 2006.
149. Kato, T., "Principle and technique of nirs-imaging for human brain force: fast-oxygen response in capillary event.," *International Congress Series*, Vol. 1270, pp. 85–90, Aug. 2004.
150. Boas, D. A., T. Gaudette, G. Strangman, X. Cheng, J. J. Marota, and J. B. Mandeville, "The accuracy of near infrared spectroscopy and imaging during focal changes in cerebral hemodynamics.," *Neuroimage*, Vol. 13, pp. 76–90, Jan 2001.
151. Chance, B., E. Anday, S. Nioka, S. Zhou, H. Long, K. Worden, C. Li, T. Turray, Y. Ovet-sky, D. Pidikiti, and R. Thomas, "A novel method for fast imaging of brain function, noninvasively, with light.," *Optics Express*, Vol. 2, p. 411i; $\frac{1}{2}$ 423, 1998.
152. Akgı, C. B., B. Sankur, and A. Akin, "Spectral analysis of event-related hemodynamic responses in functional near infrared spectroscopy.," *J Comput Neurosci*, Vol. 18, no. 1, pp. 67–83, 2005.
153. Cox, R. W., "Afni: software for analysis and visualization of functional magnetic resonance neuroimages.," *Comput Biomed Res*, Vol. 29, pp. 162–173, Jun 1996.
154. Thomason, M. E., L. C. Foland, and G. H. Glover, "Calibration of bold fmri using breath holding reduces group variance during a cognitive task.," *Hum Brain Mapp*, Vol. 28, pp. 59–68, Jan 2007.
155. Bruhn, H., A. Kleinschmidt, H. Boecker, K. D. Merboldt, W. H; $\frac{1}{2}$ icke, and J. Frahm, "The effect of acetazolamide on regional cerebral blood oxygenation at rest and under stimulation as assessed by mri.," *J Cereb Blood Flow Metab*, Vol. 14, pp. 742–748, Sep 1994.
156. Sage, J. I., R. L. V. Uitert, and T. E. Duffy, "Simultaneous measurement of cerebral blood flow and unidirectional movement of substances across the blood-brain barrier: theory, method, and application to leucine.," *J Neurochem*, Vol. 36, pp. 1731–1738, May 1981.
157. Huppert, T. J., R. D. Hoge, S. G. Diamond, M. A. Franceschini, and D. A. Boas, "A temporal comparison of bold, asl, and nirs hemodynamic responses to motor stimuli in adult humans.," *Neuroimage*, Vol. 29, pp. 368–382, Jan 2006.

158. Stillman, A. E., X. Hu, and M. Jerosch-Herold, "Functional MRI of brain during breath holding at 4 T," *J. Magn. Reson. Imaging.*, Vol. 13, pp. 893–897, 1995.
159. Moritz, C. H., M. E. Meyerand, and A. Saykin, "Bold contrast response in human brain during simple breathhold measured at 1.5 tesla," in *Proc Int Soc for Magn Reson in Med*, p. 1405, 1998.
160. Kwong, K. K., I. Wanke, K. M. Donahue, T. L. Davis, and B. R. Rosen, "Epi imaging of global increase of brain mr signal with breath-hold preceded by breathing o₂," *Magn Reson Med*, Vol. 33, pp. 448–452, Mar 1995.
161. Kastrup, A., T. Q. Li, A. Takahashi, G. H. Glover, and M. E. Moseley, "Functional magnetic resonance imaging of regional cerebral blood oxygenation changes during breath holding.," *Stroke*, Vol. 29, pp. 2641–2645, Dec 1998.
162. Peebles, K., L. Celi, K. McGrattan, C. Murrell, K. Thomas, and P. N. Ainslie, "Human cerebrovascular and ventilatory co₂ reactivity to end-tidal, arterial and internal jugular vein pco₂," *J Physiol*, Aug 2007.
163. Lee, T. S., "End-tidal partial pressure of carbon dioxide does not accurately reflect paco₂ in rabbits treated with acetazolamide during anaesthesia.," *Br J Anaesth*, Vol. 73, pp. 225–6, 1994.
164. Robbins, P. A., J. Conway, D. A. Cunningham, S. Khamnei, and D. J. Paterson, "A comparison of indirect methods for continuous estimation of arterial pco₂ in men.," *J Appl Physiol*, Vol. 68, pp. 1727–1731, Apr 1990.
165. Tojima, H., T. Kuriyama, and Y. Fukuda, "Arterial to end-tidal pco₂ difference varies with different ventilatory conditions during steady state hypercapnia in the rat.," *Jpn J Physiol*, Vol. 38, no. 4, pp. 445–457, 1988.
166. Posse, S., L. J. Kemna, B. Elghahwagi, S. Wiese, and V. G. Kiselev, "Effect of graded hypo- and hypercapnia on fmri contrast in visual cortex: quantification of t^(*)(2) changes by multiecho epi.," *Magn Reson Med*, Vol. 46, pp. 264–271, Aug 2001.
167. Hoge, R. D., J. Atkinson, B. Gill, G. R. Crelier, S. Marrett, and G. B. Pike, "Investigation of bold signal dependence on cerebral blood flow and oxygen consumption: the deoxyhemoglobin dilution model.," *Magn Reson Med*, Vol. 42, pp. 849–863, Nov 1999.
168. Kastrup, A., T. Q. Li, G. H. Glover, and M. E. Moseley, "Cerebral blood flow-related signal changes during breath-holding.," *AJNR Am J Neuroradiol*, Vol. 20, pp. 1233–1238, Aug 1999.
169. Palada, I., A. Obad, D. Bakovic, Z. Valic, V. Ivancev, and Z. Dujic, "Cerebral and peripheral hemodynamics and oxygenation during maximal dry breath-holds.," *Respir Physiol Neurobiol*, Vol. 157, pp. 374–381, Aug 2007.
170. Molinari, F., W. Liboni, G. Grippi, and E. Negri, "Relationship between oxygen supply and cerebral blood flow assessed by transcranial doppler and near - infrared spectroscopy in healthy subjects during breath - holding.," *J Neuroengineering Rehabil*, Vol. 3, p. 16, 2006.
171. de Boorder, M. J., J. Hendrikse, and J. van der Grond, "Phase Contrast Magnetic Resonance Imaging Measurements of Cerebral Autoregulation With a Breath Hold Challenge : A Feasibility Study," *Stroke*, Vol. 35, pp. 1350–1354, 2004.

172. Okada, E., M. Firbank, and D. T. Delpy, "The effect of overlying tissue on the spatial sensitivity profile of near-infrared spectroscopy," *Phys Med Biol*, Vol. 40, pp. 2093–2108, Dec 1995.
173. Vernieri, F., N. Rosato, F. Pauri, F. Tibuzzi, F. Passarelli, and P. M. Rossini, "Near infrared spectroscopy and transcranial doppler in monohemispheric stroke.," *Eur Neurol*, Vol. 41, no. 3, pp. 159–162, 1999.
174. Smielewski, P., P. Kirkpatrick, P. Minhas, J. D. Pickard, and M. Czosnyka, "Can cerebrovascular reactivity be measured with near-infrared spectroscopy?," *Stroke*, Vol. 26, pp. 2285–2292, Dec 1995.
175. Grubhofer, G., A. Lassnigg, F. Manlik, E. Marx, W. Trubel, and M. Hiesmayr, "The contribution of extracranial blood oxygenation on near-infrared spectroscopy during carotid thrombendarterectomy.," *Anaesthesia*, Vol. 52, pp. 116–120, Feb 1997.